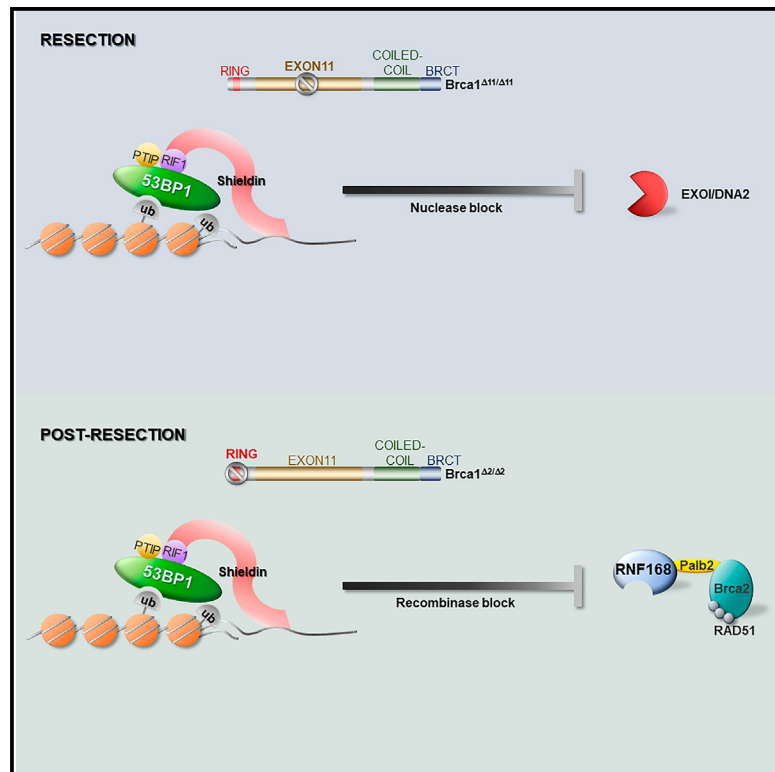


Molecular Cell

53BP1 Enforces Distinct Pre- and Post-resection Blocks on Homologous Recombination

Graphical Abstract



Authors

Elsa Callen, Dali Zong, Wei Wu, ..., Nima Mosammaparast, Peter J. McKinnon, André Nussenzweig

Correspondence

andre_nussenzweig@nih.gov

In Brief

BRCA1 promotes 5'-3' end resection and subsequently loads RAD51 onto 3' single-stranded DNA to initiate homologous recombination. Callen et al. demonstrate that 53BP1 antagonizes both key steps in homologous recombination—end resection and RAD51 loading—that are coordinated by BRCA1.

Highlights

- 53BP1^{S25A} point mutation rescues lethality of BRCA1^{Δ11} mice without restoring HR
- 53BP1^{S25A} mutation uncouples 53BP1 end-blocking activities pre- and post-resection
- RIF1/shieldin blocks BRCA1-independent loading of RAD51 onto single-strand DNA
- Shieldin and PTIP associate with 53BP1 to regulate distinct end-resection pathways



53BP1 Enforces Distinct Pre- and Post-resection Blocks on Homologous Recombination

Elsa Callen,^{1,7} Dali Zong,^{1,7} Wei Wu,¹ Nancy Wong,¹ Andre Stanlie,¹ Momoko Ishikawa,¹ Raphael Pavani,¹ Lavinia C. Dumitraci,² Andrea K. Byrum,³ Carlos Mendez-Dorantes,⁴ Paula Martinez,⁵ Andres Canela,¹ Yaakov Maman,¹ Amanda Day,¹ Michael J. Kruhlak,⁶ Maria A. Blasco,⁵ Jeremy M. Stark,⁴ Nima Mosammaparast,³ Peter J. McKinnon,² and André Nussenzweig^{1,8,*}

¹Laboratory of Genome Integrity, National Cancer Institute, NIH, Bethesda, MD 20892, USA

²Department of Genetics, St. Jude Children's Research Hospital, Memphis, TN 38105, USA

³Department of Pathology and Immunology, Washington University in St. Louis, St. Louis, MO 63110, USA

⁴Department of Cancer Genetics and Epigenetics, Beckman Research Institute of the City of Hope, Duarte, CA 91010, USA

⁵Telomeres and Telomerase Group, Molecular Oncology Program, Spanish National Cancer Center, Madrid 28029, Spain

⁶Laboratory of Cancer Biology and Genetics, National Cancer Institute, NIH, Bethesda, MD 20892, USA

⁷These authors contributed equally

⁸Lead Contact

*Correspondence: andre_nussenzweig@nih.gov

<https://doi.org/10.1016/j.molcel.2019.09.024>

SUMMARY

53BP1 activity drives genome instability and lethality in BRCA1-deficient mice by inhibiting homologous recombination (HR). The anti-recombinogenic functions of 53BP1 require phosphorylation-dependent interactions with PTIP and RIF1/shieldin effector complexes. While RIF1/shieldin blocks 5'-3' nucleolytic processing of DNA ends, it remains unclear how PTIP antagonizes HR. Here, we show that mutation of the PTIP interaction site in 53BP1 (S25A) allows sufficient DNA2-dependent end resection to rescue the lethality of *BRCA1*^{D11} mice, despite increasing RIF1 "end-blocking" at DNA damage sites. However, double-mutant cells fail to complete HR, as excessive shieldin activity also inhibits RNF168-mediated loading of PALB2/RAD51. As a result, *BRCA1*^{D11}*53BP1*^{S25A} mice exhibit hallmark features of HR insufficiency, including premature aging and hypersensitivity to PARPi. Disruption of shieldin or forced targeting of PALB2 to ssDNA in *BRCA1*^{D11}*53BP1*^{S25A} cells restores RNF168 recruitment, RAD51 nucleofilament formation, and PARPi resistance. Our study therefore reveals a critical function of shieldin post-resection that limits the loading of RAD51.

INTRODUCTION

The tumor suppressor BRCA1 coordinates two key steps during DNA double-strand break (DSB) repair by homologous recombination (HR) (Chen et al., 2018). Initially, BRCA1 pro-

motes 5'-3' end resection, and subsequently, it recruits the PALB2/BRCA2 mediator complex to load the RAD51 recombinase onto 3' single-stranded DNA (ssDNA). In BRCA1-deficient cells, HR is severely compromised, leading to genome instability during development that precipitates tumorigenesis (Chen et al., 2018). However, 53BP1 loss largely restores HR in BRCA1-deficient mice, resulting in the rescue of the embryonic lethality and the suppression of cancer predisposition in pre-clinical mouse tumor models (Bouwman et al., 2010; Bunting et al., 2010; Cao et al., 2009). The dramatic rescue of HR in BRCA1-deficient mice is in part due to the role of 53BP1 in blocking end resection (Bunting et al., 2010). However, in some cell lines, BRCA1 depletion had minimal effects on end processing under conditions in which RAD51 filament formation was compromised (Zhou et al., 2014). RAD51 filament formation in BRCA1-deficient cells requires the alternative recruitment of PALB2/BRCA2 through RNF168-mediated chromatin ubiquitylation (Zong et al., 2019). This raises the question of whether 53BP1, in addition to blocking resection, also antagonizes RNF168-driven RAD51 filament formation.

The pro-end-joining and anti-recombination functions of 53BP1 require phospho-dependent interactions with downstream effectors such as RIF1 and PTIP (Setiaputra and Durocher, 2019). Recently, independent laboratories have discovered components of a "shieldin complex," which acts downstream of RIF1 to block resection (Dev et al., 2018; Findlay et al., 2018; Gao et al., 2018; Ghezraoui et al., 2018; Gupta et al., 2018; Mirman et al., 2018; Noordermeer et al., 2018). Loss of RIF1 or shieldin leads to defective immunoglobulin class switch recombination (CSR), blocks the fusion of dysfunctional telomeres, and promotes poly ADP ribose polymerase inhibitor (PARPi) resistance in BRCA1-deficient cells (Dev et al., 2018; Findlay et al., 2018; Gao et al., 2018; Ghezraoui et al., 2018; Gupta et al., 2018; Mirman et al., 2018; Noordermeer et al.,



2018; Setiaputra and Durocher, 2019). However, RIF1 and PTIP also have essential functions in replication and transcription (Alver et al., 2017; Buonomo et al., 2009; Cho et al., 2003; Daniel et al., 2010), making their roles in 53BP1-dependent DSB repair ambiguous.

To determine the contribution of PTIP binding to 53BP1-dependent suppression of end resection and HR, we generated 53BP1-knockin mice harboring a single point mutation (S25A) in 53BP1. The 53BP1S25A mutation selectively impairs PTIP while it enhances the association of RIF1 with DSBs. The mutant 53BP1 protein is permissive for end resection sufficient to rescue the lethality of *BRCA1*^{Δ11} mice, but it nevertheless blocks RAD51 loading. Our study thereby uncovers a new role for 53BP1 in antagonizing HR at the post-resection step.

Finally, we report that distinct domains of BRCA1 are capable of counteracting anti-recombinogenic functions of 53BP1 pre- and post-resection. Thus, BRCA1 mutant cells lacking exon 11 are severely impaired in DSB resection, while the loss of the BRCA1 RING domain maintains resection capability but fails to support RAD51 foci formation. Since pathogenic germline mutations in the RING domain and exon 11 are frequently found in familial breast and ovarian cancers and may predict poor responses to chemotherapy (Drost et al., 2016; Wang et al., 2016), these results have implications for our understanding of cellular mechanisms leading to PARPi and platinum resistance.

RESULTS

53BP1S25A Mutation Increases the Association of RIF1 with DNA Breaks

To dissect the contribution of phospho-dependent 53BP1-PTIP interaction to DSB repair in a physiological setting that does not compromise replication, MLL3/4 methyltransferase activity (Gong et al., 2009; Ray Chaudhuri et al., 2016), or 53BP1-dependent p53 activation (Cuello-Martin et al., 2016), we replaced serine 25 with alanine in embryonic stem cells (Figure S1A), which were used to generate 53BP1^{S25A} mice. As expected, homozygous mutant 53BP1^{S25A} mice were born at normal Mendelian frequencies and did not exhibit any overt phenotype (Figure S1A; data not shown). 53BP1 protein was present at normal levels but irradiation-induced S25 phosphorylation, which is largely ATM dependent, was absent in 53BP1^{S25A} mice (Figures S1B and S1C). Notably, irradiation-induced foci (IRIF) for RIF1 were significantly elevated in 53BP1^{S25A} MEFs (Figure 1A), while PTIP recruitment to DSBs was undetectable in mutant cells (Figure 1B). Consistent with these findings, analysis by mass spectrometry revealed that RIF1 peptides were enriched and PTIP peptides were depleted in 53BP1 immunoprecipitates from cells expressing 53BP1^{S25A} compared to 53BP1^{WT} (Figures 1C and 1D; Table S1). Thus, the 53BP1S25A mutation specifically impairs PTIP while enhancing the association of RIF1 with DNA breaks. Conversely, it was shown that the mutation of seven N-terminal phosphorylation sites in 53BP1 that decreased RIF1-53BP1 association led to a concomitant increase in PTIP-53BP1 interaction (Callen et al., 2013).

53BP1S25A Rescues the Lethality of *BRCA1*^{Δ11} Mice but Leads to Premature Aging

The complete loss of 53BP1 is thought to rescue the embryonic lethality of BRCA1-deficient mice by increasing DSB resection (Bunting et al., 2010) and by permitting RNF168-mediated loading of RAD51 onto ssDNA (Zong et al., 2019). To examine the relative contribution of each of these processes to embryonic viability, we crossed 53BP1^{S25A} mice with mice expressing a mutant form of BRCA1 where exon 11 is deleted. While homozygous *BRCA1*^{Δ11} mutation is incompatible with viability, we found that *BRCA1*^{Δ11}53BP1^{S25A} mice were born at expected Mendelian frequencies and reached adulthood (Figures 2A and 2B). Similar to *BRCA1*^{Δ11}53BP1^{−/−} mice (Bunting et al., 2010), mutant males were sterile and showed reduced testes size (Figure S2A), most likely reflecting the role of BRCA1 in meiotic sex chromosome inactivation (Turner et al., 2005). However, in striking contrast to *BRCA1*^{Δ11}53BP1^{−/−} mice, which exhibit a normal lifespan (Bunting et al., 2010), *BRCA1*^{Δ11}53BP1^{S25A} mice died prematurely, with a median survival of 6 months and a maximum lifespan of 92 weeks (Figure 2B). *BRCA1*^{Δ11}53BP1^{S25A} mice developed pathologies that are consistent with accelerated aging, including kyphosis, blindness, inflammation, hair graying, and overall reduced activity, with only a modest rate of cancer formation (<10%) (Figures 2C and S2B). Thus, a single-point mutation in 53BP1 disrupting PTIP binding is sufficient to fully rescue the prenatal lethality of *BRCA1*^{Δ11} mice, but it is insufficient to allow normal organismal aging.

Premature aging could be due to elevated DNA damage signaling leading to senescence and apoptosis (Niedernhofer et al., 2018). Already at embryonic day 13.5 (E13.5), *BRCA1*^{Δ11}53BP1^{S25A} embryos appear smaller than wild type (WT) (Figure 2D), and mutant primary murine embryonic fibroblasts (MEFs) prematurely senesced at the same rate as *BRCA1*^{Δ11} cells (Figure 2E). Various tissues from mutant embryos, including cerebellum, liver, and limb, showed TUNEL⁺ and caspase 3⁺ staining indicative of apoptosis (Figure S2C); and increased apoptosis was associated with enhanced levels of DNA damage signaling, as measured by Kap1 phosphorylation (Figure S2D). Consistent with the increased neural apoptosis, mutant mice had a smaller brain, although its overall structure was undisturbed (Figure S2E). Thus, despite the loss of embryonic cells *in vivo* and poor growth *in vitro*, the rescue of viability in *BRCA1*^{Δ11}53BP1^{S25A} mice was associated with normal developmental processes but accelerated postnatal aging.

Cells from *BRCA1*^{Δ11}53BP1^{S25A} Mice Are Severely Compromised for RAD51 Loading

Because RAD51-dependent HR is largely rescued in *BRCA1*^{Δ11} mice lacking 53BP1, mutant cells are resistant to PARPi and show robust RAD51 foci formation (Bunting et al., 2010). In striking contrast, *BRCA1*^{Δ11}53BP1^{S25A} mice (n = 3) died within 9 days after treatment with PARPi. Histological analysis revealed severe injuries to the gastrointestinal tract, including the blunting of villi and the almost complete obliteration of stem cell crypts (Figure 3A). Consistent with the *in vivo* response, mutant B cells

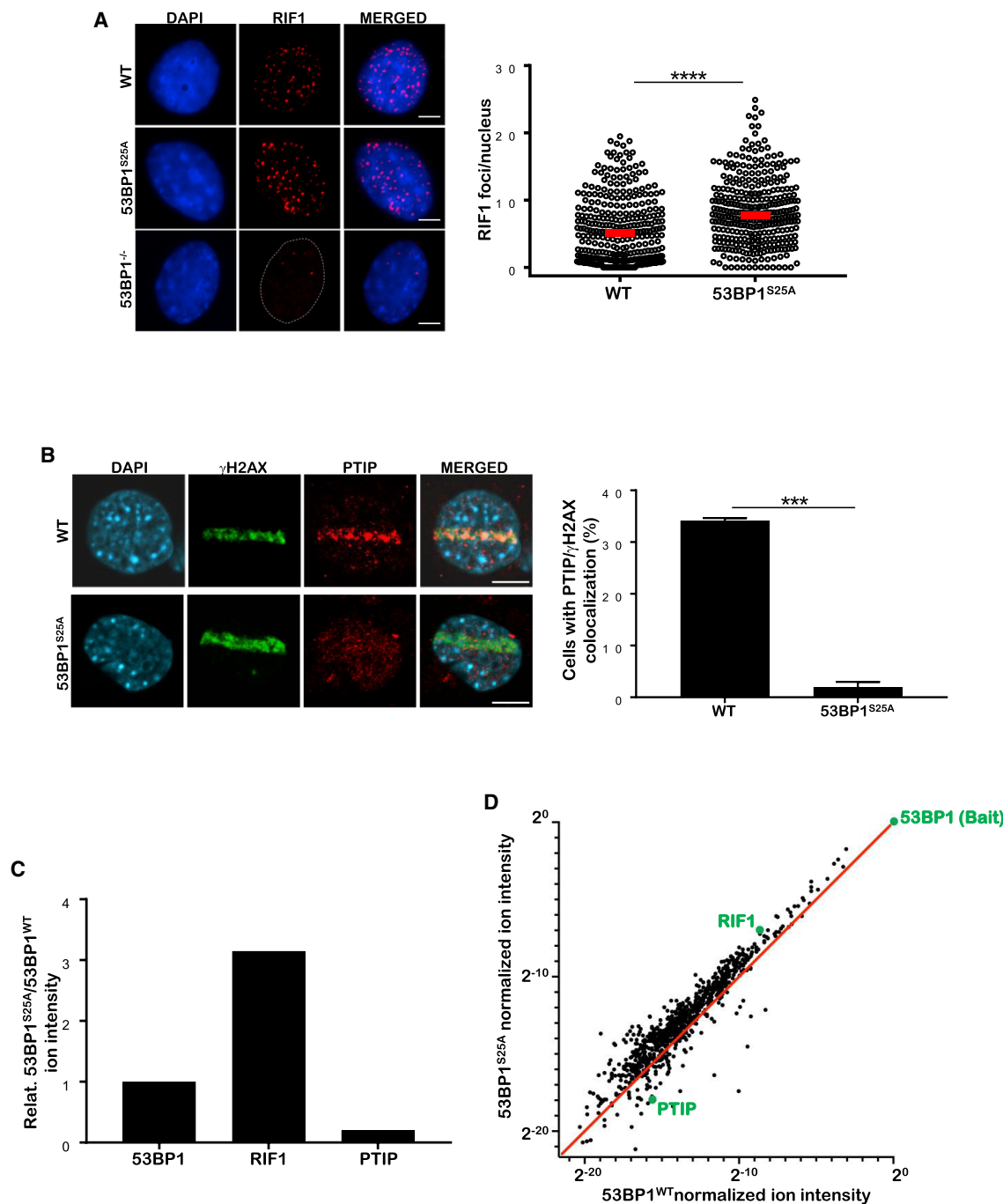


Figure 1. Serine 25 to Alanine Mutation in 53BP1 Compromises PTIP Binding while Increasing RIF1 Association at DSBs

(A) Left: WT, $53BP1^{-/-}$ and $53BP1^{S25A}$ MEFs were assayed for RIF1 (red) IRIF (10 Gy, 1 h recovery). Cells were counterstained with DAPI (blue). Scale bar represents 10 μ m. Right: quantification of RIF1 foci per nucleus in WT and $53BP1^{S25A}$ MEFs, normalized by nuclear area (per 100 μ m²). A minimum of 300 nuclei were quantified per condition using Gen5 spot analysis software. A representative experiment ($n = 3$) is shown. Statistical significance was determined by the Mann-Whitney t test.

(B) Left: PTIP (red) recruitment to laser microirradiation damage in WT and $53BP1^{S25A}$ MEFs. Damaged cells are indicated by γ -H2AX tracks (green). Scale bar represents 10 μ m. Right: quantification of cells with PTIP/ γ -H2AX colocalization. Statistical significance was determined by the Mann-Whitney t test.

(C and D) Graphs depicting the relative ion intensities for 53BP1, RIF1, and PTIP peptides associated with the 53BP1 complex in HeLa-S cells expressing FLAG-HA-53BP1^{S25A} or FLAG-HA-53BP1^{WT}, as determined by mass spectrometry.

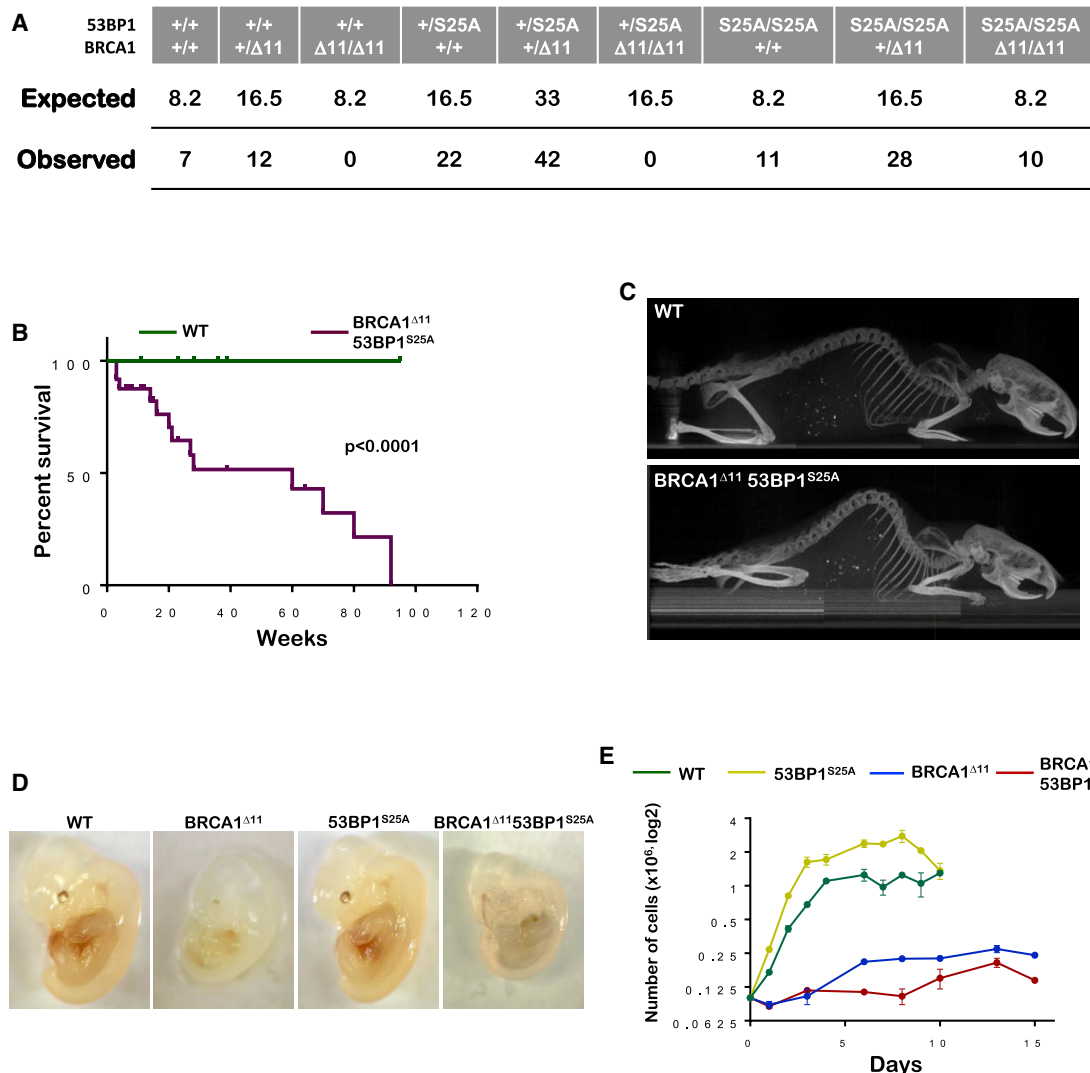


Figure 2. 53BP1S25A Mutation Reverts the Lethality of *BRCA1* Δ^{11} Mice but Promotes Accelerated Aging and an Elevated Rate of Senescence

(A) Table showing the expected and observed frequency of breeding outcomes from *BRCA1* $^{+/+}$ *53BP1* $^{+/S25A}$ x *BRCA1* $^{+/+}$ *53BP1* $^{+/S25A}$ intercrosses.

(B) Kaplan-Meier survival analysis of WT and *BRCA1* Δ^{11} *53BP1* S^{25A} mice (n = 14). A significantly shorter lifespan was observed in *BRCA1* Δ^{11} *53BP1* S^{25A} mice compared to WT (p < 0.0001). The log-rank (Mantel-Cox) test was used to determine the statistical significance.

(C) Representative X-ray CT projection image showing increased kyphosis in a 4-month-old *BRCA1* Δ^{11} *53BP1* S^{25A} mouse compared with a WT littermate.

(D) Representative image of E13.5 WT, *BRCA1* Δ^{11} , *53BP1* S^{25A} , and *BRCA1* Δ^{11} *53BP1* S^{25A} embryos showing the decrease in size of *BRCA1* Δ^{11} and *BRCA1* Δ^{11} *53BP1* S^{25A} animals.

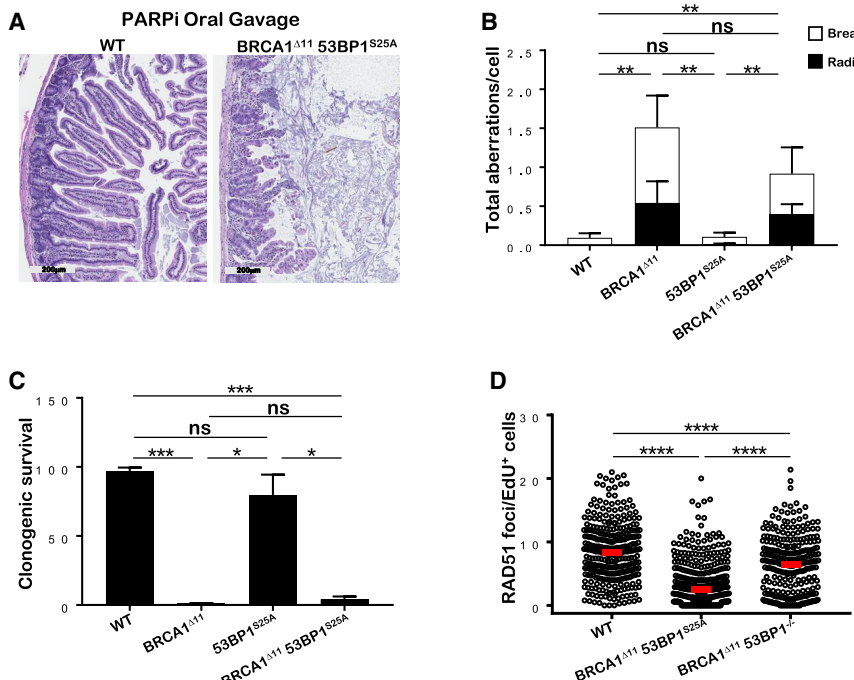
(E) *In vitro* growth of primary WT, *BRCA1* Δ^{11} , *53BP1* S^{25A} , and *BRCA1* Δ^{11} *53BP1* S^{25A} MEFs at passage 2.

and MEFs showed hypersensitivity to PARPi, as indicated by the elevated induction of chromosomal aberrations and increased formation of radials (Figures 3B and S3A). Mutant MEFs also showed a marked reduction in colony growth after PARPi treatment (Figure 3C). Moreover, we observed a severe impairment in ionizing radiation (IR)-induced RAD51 foci formation in *BRCA1* Δ^{11} *53BP1* S^{25A} MEFs and B cells (Figures 3D and S3B). Notably, the HR defect is more severe in *BRCA1* Δ^{11} *53BP1* S^{25A} cells compared to that observed in *BRCA1*/PTIP-deficient cells (Callen et al., 2013), suggesting that PTIP has additional roles within the MLL3/4 complex independent of its interaction with

53BP1 (Ray Chaudhuri et al., 2016). Moreover, in contrast to 53BP1 ablation (Bunting et al., 2010), the 53BP1S25A mutation rescues the lethality of *BRCA1* Δ^{11} mice without restoring HR. Our results therefore indicate that severely reduced HR is compatible with viability but leads to premature aging.

53BP1S25A Mutation Increases End Resection in *BRCA1* Δ^{11} Cells

We speculated that the mutant 53BP1S25A protein may allow end resection sufficient to rescue the lethality of *BRCA1* Δ^{11} mice, but inadequate for robust RAD51 foci formation or



(D) RAD51 foci per 5-ethynyl-2'-deoxyuridine (EdU) positive nucleus in WT, *BRCA1*^{Δ11}53BP1^{S25A}, and *BRCA1*^{Δ11}53BP1^{−/−} MEFs measured 4 h after 10 Gy IR, normalized by nuclear area (per 100 μm^2).

A minimum of 300 nuclei were quantified using Gen5 spot analysis software. A representative experiment ($n = 2$) is shown. Statistical significance was determined by the Mann-Whitney t test.

resistance to PARPi. To quantitate the level of end resection, we generated site-specific DSBs by inducible expression of the restriction enzyme AsiSI and performed END-seq, which maps the double-stranded DNA (dsDNA)/ssDNA junctions at DSB sites (Canela et al., 2016). We observed considerable variation in resection across individual sites targeted by AsiSI (Figures 4A and S4A). Levels of end resection increased with breakage, which in turn correlated with active chromatin marks (Figures S4B and S4C) (Aymard et al., 2014). By visual inspection, it was clear that MEFs derived from 53BP1^{−/−} mice exhibited increased end resection relative to WT, whereas *BRCA1*^{Δ11} MEFs showed reduced nucleolytic processing at all DSB sites (Figures 4A and S4A). The measurement of RPA-bound ssDNA by chromatin immunoprecipitation sequencing (ChIP-seq) (Brick et al., 2018), although less sensitive than END-seq, confirmed these findings (Figures 4A and S4D).

53BP1^{S25A} mutant MEFs showed slightly longer resection tracts than WT (Figure 4B and S4E). Consistently, we observed mildly increased levels of chromatin-bound RPA in mutant cells (Figure S4F). Moreover, single-strand annealing (SSA), a mutagenic RAD51-independent homology-mediated repair pathway that requires end resection (Stark et al., 2004), was slightly elevated (1.4-fold) in 53BP1^{S25A} cells (Figure S4G). The average resection length in *BRCA1*^{Δ11}53BP1^{−/−} MEFs was similar to WT and intermediate between 53BP1 and *BRCA1* deficiency (Figure 4B). Despite severely compromised IR-induced RAD51 foci (Figure 3D), *BRCA1*^{Δ11}53BP1^{S25A} MEFs accumulated elevated levels of ssDNA at AsiSI sites relative to *BRCA1*^{Δ11} or WT (Figure

Figure 3. *BRCA1*^{Δ11}53BP1^{S25A} Mice Are Sensitive to PARPi and Defective in RAD51 Filament Assembly

(A) Representative histological images of the small intestine of *BRCA1*^{Δ11}53BP1^{S25A} and WT littermate controls upon treatment with PARPi by daily oral gavage. Image was taken 9 days after treatment. In *BRCA1*^{Δ11}53BP1^{S25A} mice, small intestinal villi are blunted and fused and the lamina propria is expanded by increased inflammatory cells; intestinal crypts are unorganized, and cells display atypia.

(B) Genomic instability (chromosome breaks and radials) measured in metaphase spreads from B lymphocytes derived from WT, *BRCA1*^{Δ11}, 53BP1^{S25A}, and *BRCA1*^{Δ11}53BP1^{S25A} mice after PARPi treatment. Cells were stimulated for 2 days and then treated for 16 h with 1 μM PARPi. At least 50 cells were scored per condition. The experiment was repeated five times. Statistical significance was determined by the Mann-Whitney t test.

(C) Colony formation in WT, *BRCA1*^{Δ11}, 53BP1^{S25A}, and *BRCA1*^{Δ11}53BP1^{S25A} MEFs measured 9 days after continual treatment with 1 μM PARPi. Data are plotted relative to the plating efficiency of untreated controls of the same genotype. Statistical significance was determined by the Mann-Whitney t test.

ure 4B). Moreover, IR-induced chromatin binding of RPA was increased in *BRCA1*^{Δ11}53BP1^{S25A} cells (Figure S4F). Thus, disrupting the 53BP1-PTIP interaction largely rescues the end resection defect associated with *BRCA1* deficiency, but *BRCA1*^{Δ11}53BP1^{S25A} cells are nevertheless defective in loading RAD51.

End Resection Is Predominantly Catalyzed by DNA2 in *BRCA1*^{Δ11}53BP1^{S25A} Cells

The nucleases EXO1 and DNA2 are thought to act redundantly to promote end resection (Symington, 2016). Consistently, whereas depletion of EXO1 alone or treatment with the chemical inhibitor of DNA2 (NSC-105808) by itself did not decrease IR-induced RPA chromatin binding in replicating WT cells, end resection was significantly decreased when both nucleases were inactivated simultaneously (Figure 4C). However, in *BRCA1*^{Δ11}53BP1^{S25A} cells, treatment with DNA2 inhibitor (DNA2i) alone significantly reduced IR-induced RPA recruitment to damaged sites, while EXO1 inhibition had a smaller impact (Figure 4D). Similarly, BLM inhibition (BLMI) significantly reduced RPA foci formation in *BRCA1*^{Δ11}53BP1^{S25A} cells relative to WT (Figure S4H). These data implied that DNA2 activity is normally blocked by the 53BP1-PTIP interaction. To determine which machinery catalyzes end resection in the absence of shieldin, we examined nucleolytic processing in *BRCA1*^{Δ11}SHLD3^{−/−} cells and in *BRCA1*^{Δ11} cells depleted for RIF1. In contrast to *BRCA1*^{Δ11}53BP1^{S25A} cells, DNA damage induced RPA chromatin binding in *BRCA1*^{Δ11}SHLD3^{−/−}, and

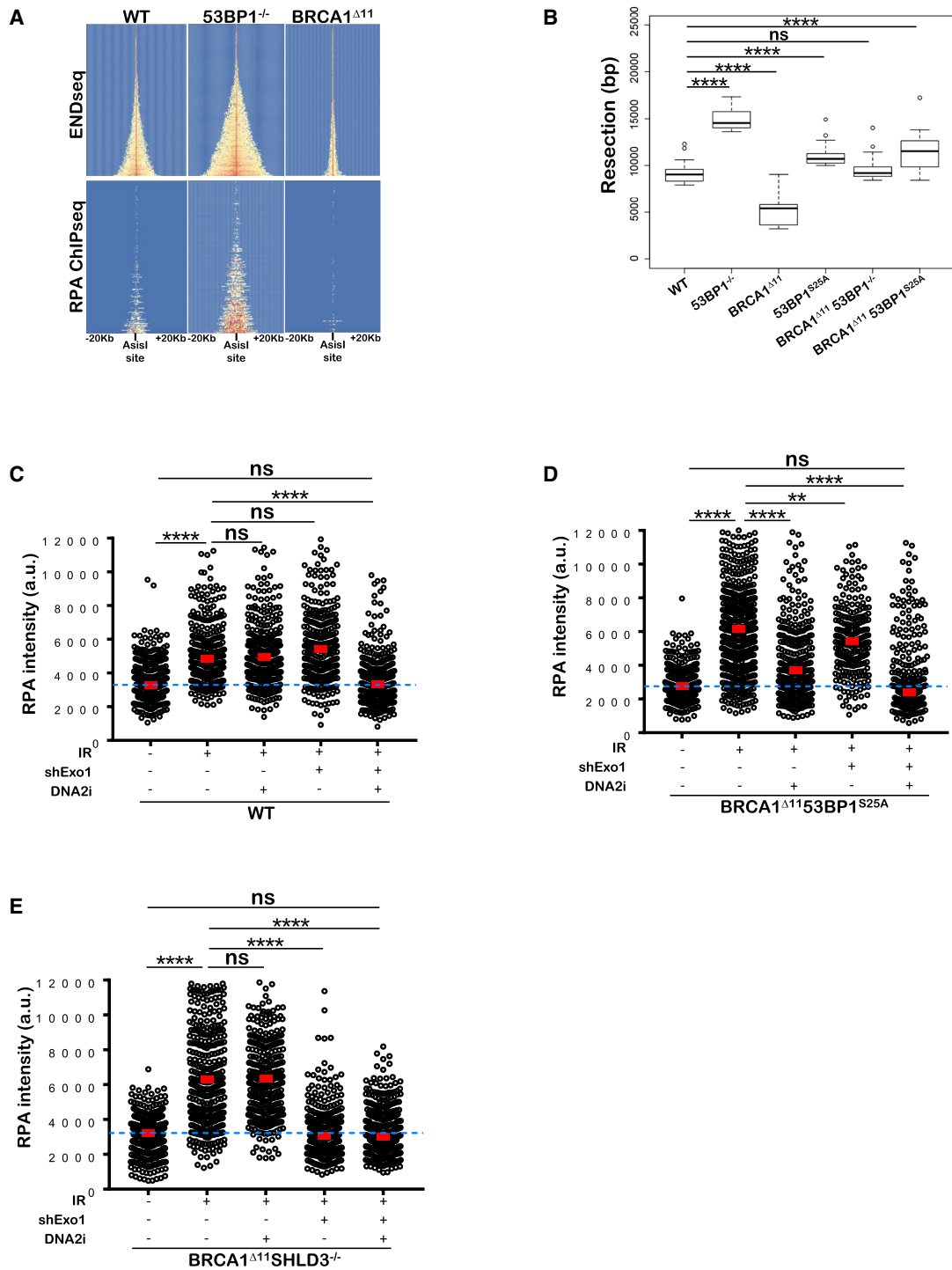


Figure 4. $BRCA1^{\Delta 11} 53BP1^{S25A}$ Cells Exhibit Normal Levels of End Resection Catalyzed Mainly by DNA2i

(A) Top panel: heatmap of END-seq signals across individual Asil sites in WT, $53BP1^{-/-}$, and $BRCA1^{\Delta 11}$ MEFs measured 5 h after Asil induction. Lower panel: ChIP-seq for ssDNA bound by RPA in the same cells. Heatmaps are ordered by END-seq signal intensity in WT cells.

(B) Boxplots showing the quantification of resection endpoints in the top 10% resected breaks in WT, $53BP1^{-/-}$, $BRCA1^{\Delta 11}$, $53BP1^{S25A}$, $BRCA1^{\Delta 11} 53BP1^{-/-}$, and $BRCA1^{\Delta 11} 53BP1^{S25A}$ MEFs at Asil-cleaved DSB sites. Welch's t test was used to determine statistical significance.

(C) Quantification of the intensity of chromatin-bound RPA in individual EdU-positive nuclei from WT and EXO1-depleted MEFs, either pre-treated or not with 1 μ M DNA2i before 10 Gy IR. Cells were analyzed 4 h post-IR.

(legend continued on next page)

BRCA1^{Δ11}/RIF1-depleted cells were largely dependent on EXO1 (Figures 4E and S4I). Thus, distinct domains in 53BP1 recruit effectors to suppress resection by different nucleases.

Shieldin Interferes with RAD51 Loading in *BRCA1^{Δ11}53BP1^{S25A}* Cells

To explain the apparent inability of *BRCA1^{Δ11}53BP1^{S25A}* cells to load RAD51 despite the abundant generation of ssDNA, we speculated that the RIF1/shieldin complex may directly interfere with RAD51 filament formation in *BRCA1^{Δ11}53BP1^{S25A}* cells. Similar to the *53BP1^{S25A}* single mutant (Figure 1A), *BRCA1^{Δ11}53BP1^{S25A}* MEFs showed significantly elevated levels of RIF1 foci after IR (Figure S5A). To test the role of shieldin in limiting RAD51 foci formation on resected DNA ends, we depleted Shld3 in *BRCA1^{Δ11}53BP1^{S25A}* MEFs both by small interfering RNA (siRNA)- and CRISPR/Cas9-mediated deletion. Notably, IR-induced RAD51 foci were restored when Shld3 was depleted from *BRCA1^{Δ11}53BP1^{S25A}* MEFs by either method (Figures 5A and S5B). Moreover, Shld3 depletion suppressed PARPi hypersensitivity in *BRCA1^{Δ11}53BP1^{S25A}* MEFs (Figures 5B and S5C). We conclude that shieldin blocks RAD51 filament formation post-resection in *BRCA1^{Δ11}53BP1^{S25A}* cells.

SHLD2 features oligonucleotide/oligosaccharide binding (OB) fold domains that bind to ssDNA (Dev et al., 2018; Findlay et al., 2018; Gao et al., 2018; Ghezraoui et al., 2018; Gupta et al., 2018; Mirman et al., 2018; Noordermeer et al., 2018). Forced targeting of SHLD2 to DSBs (by fusing SHLD2 to the RNF8 FHA domain) was found to suppress RAD51 foci formation in *BRCA1/53BP1*-deficient cells in a manner dependent on the SHLD2 OB fold (Noordermeer et al., 2018). Similarly, we found that the expression of FHA-SHLD2 was sufficient to reduce IR-induced RAD51 foci in WT cells only when the OB fold of SHLD2 was intact (Figure 5C). However, FHA-SHLD2 did not block IR-induced RPA foci formation (Figure 5C). Thus, in the presence of RPA-bound ssDNA, the loading of RAD51 is inhibited when SHLD2 is targeted to chromatin.

Since RNF168-dependent PALB2 recruitment is essential for loading RAD51 in *BRCA1/53BP1*-deficient cells (Zong et al., 2019), we examined PALB2 foci formation in *BRCA1^{Δ11}53BP1^{S25A}* cells by the stable overexpression of GFP-PALB2. While IR-induced PALB2 foci were readily detectable in WT cells, PALB2 foci formation was severely compromised in *BRCA1^{Δ11}53BP1^{S25A}* cells (Figures 5D and S5D). Moreover, PALB2 overexpression did not overcome the defect in RAD51 foci formation (Figure 5E). Based on these findings, we speculated that RIF1/shieldin interferes with PALB2/BRCA2 loading on ssDNA, which prevents efficient RAD51 filament formation in *BRCA1^{Δ11}53BP1^{S25A}* cells.

To test this, we targeted PALB2 to chromatin by fusing PALB2 to the FHA domain of RNF8 (FHA-PALB2) (Zong et al., 2019). Previously, we showed that forced PALB2 targeting

to resected DSBs overcomes the severe HR defect in *BRCA1^{Δ11/+}RNF168^{-/-}* cells (Zong et al., 2019). While FHA-PALB2 failed to rescue IR-induced RAD51 foci in resection-deficient *BRCA1^{Δ11}* cells, it restored RAD51 foci formation to WT levels in *BRCA1^{Δ11}53BP1^{S25A}* cells that are proficient in end resection (Figures 5E and S5E). Similarly, whereas FHA-PALB2 failed to mitigate PARPi sensitivity in *BRCA1^{Δ11}* cells or enhance PARPi resistance in *BRCA1^{Δ11}53BP1^{-/-}* cells, it markedly reduced the sensitivity of *BRCA1^{Δ11}53BP1^{S25A}* cells to PARPi (Figures 5F and 5G). PALB2 chromatin targeting also significantly reduced RIF1 foci formation (Figure 5H), which is consistent with the idea that elevated RIF1/shieldin activity blocks PALB2 function in *BRCA1^{Δ11}53BP1^{S25A}* cells. Finally, the ability of FHA-PALB2 to rescue PARPi resistance and RAD51 foci formation in *BRCA1^{Δ11}53BP1^{S25A}* was dependent on its BRCA2-interaction domain (WD40) but not its chromatin association motif (ChAM) (Figures S5F and S5G), which is consistent with the idea that PALB2 recruits and is reliant on BRCA2 to assemble RAD51 (Kowalczykowski, 2015).

To directly examine RAD51 loading on ssDNA, we performed chromatin immunoprecipitation of ssDNA-bound RAD51 (Brick et al., 2018) at AsiSI-cleaved sites. Consistent with immunofluorescence analyses, forced targeting of PALB2 to chromatin permitted RAD51 loading onto 3' ssDNA in *BRCA1^{Δ11}53BP1^{S25A}* cells, while it did not nucleate RAD51 filaments at DSB sites in *BRCA1^{Δ11}* cells (Figures 5I and S5H), presumably because of the lack of sufficient ssDNA. Thus, the post-resection HR defect in *BRCA1^{Δ11}53BP1^{S25A}* cells is caused by an inability to recruit PALB2/BRCA2 to damaged chromatin.

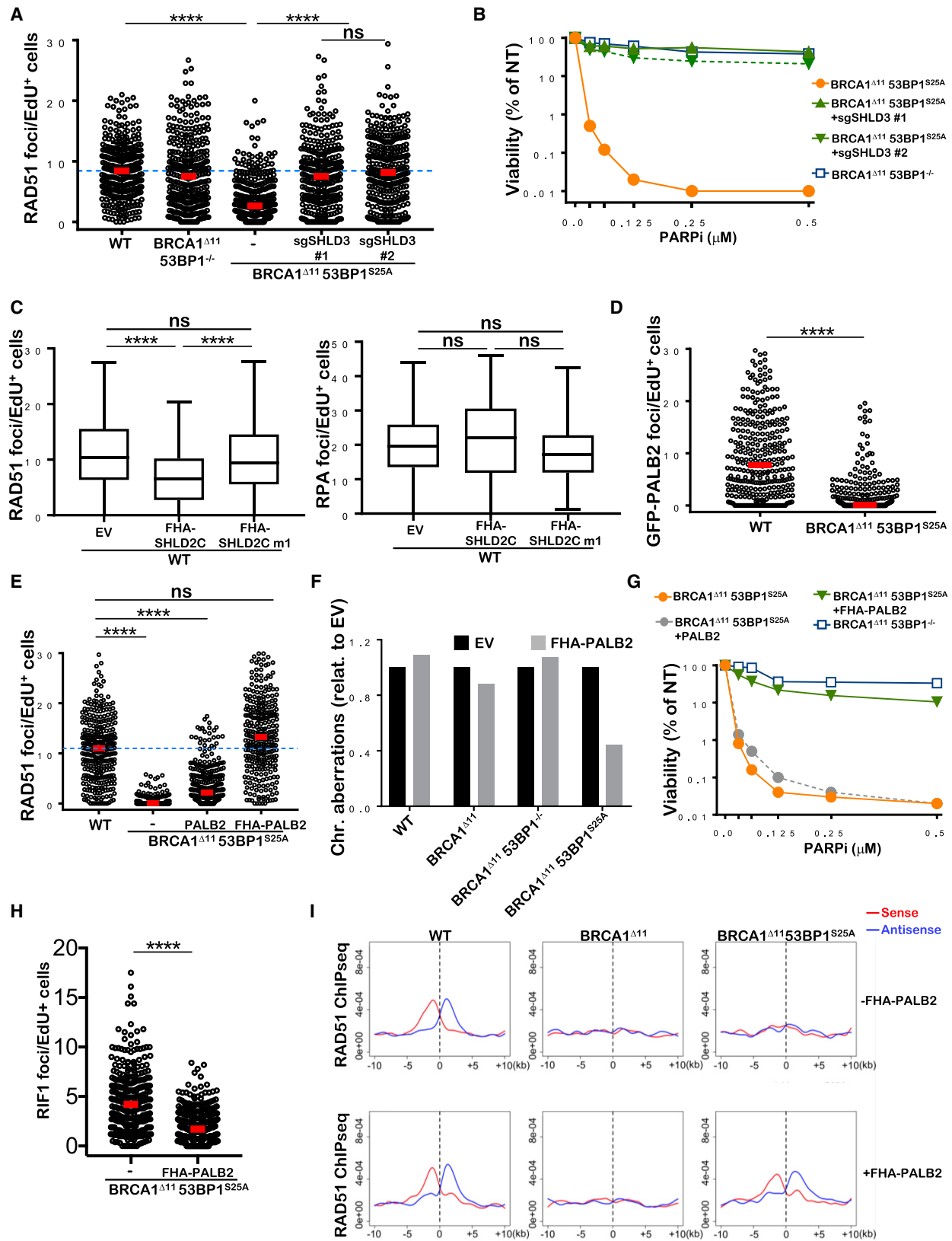
Shieldin Interferes with the RNF168 Ubiquitylation Pathway that Loads RAD51

We have recently shown that in addition to its requirement for initiating 53BP1 recruitment to DSBs early after DNA damage, the E3 ubiquitin ligase RNF168 acts redundantly with BRCA1 to load PALB2/RAD51 on resected DNA ends (Zong et al., 2019). We found that the accumulation of RNF168 at DSB sites during S phase is dependent on end resection, as it is abrogated in *BRCA1*-deficient cells and in WT cells deficient in EXO1/DNA2 (Figures 6A and 6B). Moreover, RNF168 loading in S phase is dependent on ATR signaling, as it is severely compromised when cells are pretreated with ATR inhibitor (ATRi) (Figure 6C). Because 53BP1 associates with shieldin on H2A-K15-Ub (Setiaputra and Durocher, 2019), which is also recognized by RNF168 (Doil et al., 2009; Stewart et al., 2009), we hypothesized that the block in PALB2 loading in *BRCA1^{Δ11}53BP1^{S25A}* cells may be due to the defective association of RNF168 with its own mark post-resection. The accumulation of RNF168 foci observed at 4 h after IR was severely compromised in S phase *BRCA1^{Δ11}53BP1^{S25A}* cells, whereas the initial RNF168 recruitment, necessary for

(D) Quantification of the intensity of chromatin-bound RPA in individual EdU-positive nuclei from EXO1-proficient and EXO1-depleted *BRCA1^{Δ11}53BP1^{S25A}* MEFs, either pre-treated or not with 1 μM DNA2i before 10 Gy IR. Cells were analyzed 4 h post-IR.

(E) Quantification of the intensity of chromatin-bound RPA in individual EdU-positive nuclei from EXO1-proficient and EXO1-depleted *BRCA1^{Δ11}SHLD3^{-/-}* MEFs, either pre-treated or not with 1 μM DNA2i before 10 Gy IR. Cells were analyzed 4 h post-IR.

In (C)–(E), a minimum of 300 nuclei per condition were quantified using Gen5 spot analysis software. A representative experiment (n = 2) is shown. Statistical significance was determined by the Mann-Whitney t test.



(legend on next page)

53BP1/RIF1/shieldin deposition was not altered (Figures 6D and 6E). RAD18, which binds H2A-K15-Ub produced by RNF8/RNF168 (Hu et al., 2017; Huang et al., 2009; Panier et al., 2012), also showed defective IRIF in S phase *BRCA1*^{Δ11}*53BP1*^{S25A} cells 4 h post-IR (Figures 6F and 6H). The deletion of Shld3 in *BRCA1*^{Δ11}*53BP1*^{S25A} rescued both RNF168 and RAD18 recruitment (Figures 6G and 6H). Thus, shieldin blocks the RNF168-mediated chromatin ubiquitylation pathway in *BRCA1*^{Δ11}*53BP1*^{S25A} cells post-resection, thereby compromising BRCA1-independent HR.

RING-less BRCA1 Supports End Resection but Not RAD51 Loading

The RING domain of BRCA1 possesses ubiquitin ligase activity and is required for stable interaction with BARD1 (Baer and Ludwig, 2002). Deletion of BRCA1 exon 2 (*BRCA1*^{Δ2}) results in an alternative translation initiation producing an N-terminally truncated BRCA1 protein lacking the RING domain (RING-less BRCA1) (Drost et al., 2016; Li et al., 2016; Wang et al., 2016). RING-less BRCA1 fails to stabilize BARD1 and is defective for HR (Drost et al., 2016; Li et al., 2016; Wang et al., 2016; Zong et al., 2019). In contrast to *BRCA1*^{Δ11}, we found that *BRCA1*^{Δ2} MEFs exhibited robust levels of DSB resection measured by RPA foci, but failed to form RAD51 foci (Figure 7). Since the loss of 53BP1 or RNF168 rescues the RAD51 loading defect in *BRCA1*^{Δ2} cells (Zong et al., 2019), this indicates that 53BP1 primarily blocks RAD51 loading post-resection in cells expressing mutant BRCA1 lacking the RING domain.

DISCUSSION

Our study supports a model in which RIF1/shieldin and PTIP associate independently with 53BP1 to regulate distinct end-resection pathways. Although they interact with different phosphorylation sites on 53BP1, RIF1 and PTIP appear to partially occlude each other. This results in the observed increase in IRIF for RIF1 in *53BP1*^{S25A} mutant cells that are incapable of binding PTIP. Nevertheless, elevated RIF1/shieldin activity at DSBs is insufficient to inhibit end resection on its own. Long-range resection is normally mediated by a combination of

EXO1 and DNA2, but it is catalyzed predominantly by DNA2 in PTIP-defective *BRCA1*^{Δ11}*53BP1*^{S25A} cells (Figures 4D and S6) and by EXO1 in shieldin-defective *BRCA1*^{Δ11}*SHLD3*^{−/−} or *BRCA1*^{Δ11}/RIF1-depleted cells (Figures 4E and S6). Thus, mutually exclusive phosphorylation-mediated interactions with PTIP and RIF1/shieldin enable 53BP1 to independently suppress end resection by distinct nucleases.

Although the loss of either 53BP1 effector restores end resection to normal levels in BRCA1-deficient cells, they differentially affect the downstream steps of HR. In *BRCA1*^{Δ11}*53BP1*^{S25A} cells, the continued presence of shieldin on chromatin post-resection greatly reduces the loading of RAD51 on ssDNA (Figure S6). Defective RAD51 loading may in turn promote further hyperresection in *BRCA1*^{Δ11}*53BP1*^{S25A} cells. Inefficient RAD51 filament assembly is apparently sufficient to rescue the prenatal lethality associated with *BRCA1*^{Δ11} mutation, but it is inadequate to support the normal lifespan in *BRCA1*^{Δ11}*53BP1*^{S25A} mice, even though the cancer rate is not markedly increased. These phenotypes are reminiscent of dominant-negative RAD51 mutations found in Fanconi anemia, which do not produce the typical features of bone marrow failure or cancer predisposition, but instead cause neuronal defects, microcephaly, and sensitivity to DNA-damaging agents (Ameziane et al., 2015; Takenaka et al., 2019; Wang et al., 2015).

How does 53BP1/shieldin block RAD51 filament assembly? RAD51 recombinase activity is facilitated by numerous proteins, including BRCA2, RAD54, and the family of RAD51 paralogs, which act at different stages of HR (Kowalczykowski, 2015). BRCA2 must first displace RPA from resected DNA ends to enable the subsequent deposition of RAD51 on ssDNA (Kowalczykowski, 2015). Shieldin, RPA, and BRCA2/PALB2 are OB fold-containing complexes with ssDNA-binding activity (Setiaputra and Durocher, 2019). An interesting possibility is that RPA and shieldin may form mixed polymers on ssDNA. Although BRCA2 has a higher affinity for ssDNA than RPA, it is possible that BRCA2 cannot efficiently displace shieldin to allow the nucleation of the RAD51 filament. We show that forced targeting of SHLD2 to DSBs is inhibitory to the replacement of RPA by RAD51 (Figure 5C). Nevertheless, the block in HR in *BRCA1*^{Δ11}*53BP1*^{S25A} cells, associated with the elevation

Figure 5. RAD51 Loading Defect in *BRCA1*^{Δ11}*53BP1*^{S25A} Cells Is Corrected by Shld3 Depletion or Forced PALB2 Chromatin Binding

- (A) RAD51 foci per EdU-positive nucleus in WT, *BRCA1*^{Δ11}*53BP1*^{−/−}, *BRCA1*^{Δ11}*53BP1*^{S25A}, and *BRCA1*^{Δ11}*53BP1*^{S25A} MEFs deficient in SHLD3 measured 4 h after 5 Gy IR. Two independent *BRCA1*^{Δ11}*53BP1*^{S25A}*SHLD3*^{−/−} clones (#1 and #2) were used. Foci numbers are normalized by nuclear area (per 100 μm^2).
 - (B) Viability of WT, *BRCA1*^{Δ11}*53BP1*^{S25A}, and *BRCA1*^{Δ11}*53BP1*^{S25A}*SHLD3*^{−/−} MEFs measured by CellTiter-Glo 10 days after PARPi treatment.
 - (C) RAD51 (left panel) and RPA (right panel) foci formation 4 h after 10 Gy IR in WT cells expressing FHA-SHLD2 containing (SHLD2C) or lacking (SHLD2Cm1) the OB fold (Noordermeer et al., 2018).
 - (D) GFP-PALB2 foci per EdU-positive nucleus in WT and *BRCA1*^{Δ11}*53BP1*^{S25A} MEFs overexpressing PALB2 measured 4 h after 5 Gy IR.
 - (E) RAD51 foci per EdU-positive nucleus in WT, *BRCA1*^{Δ11}*53BP1*^{S25A}, and *BRCA1*^{Δ11}*53BP1*^{S25A} MEFs overexpressing PALB2 or PALB2 fused with the FHA domain of RNF8, measured 4 h after 10 Gy IR. Foci numbers are normalized by nuclear area (per 100 μm^2).
 - (F) Chromosomal aberrations in WT, *BRCA1*^{Δ11}, *BRCA1*^{Δ11}*53BP1*^{−/−}, and *BRCA1*^{Δ11}*53BP1*^{S25A} expressing empty vector or FHA-PALB2.
 - (G) Viability of *BRCA1*^{Δ11}*53BP1*^{S25A} and *BRCA1*^{Δ11}*53BP1*^{−/−} MEFs with or without ectopic FHA-PALB2 protein expression measured by CellTiter-Glo 10 days after PARPi treatment.
 - (H) RIF1 foci per EdU-positive nucleus in *BRCA1*^{Δ11}*53BP1*^{S25A} and *BRCA1*^{Δ11}*53BP1*^{S25A} MEFs expressing FHA-PALB2 measured 4 h after 10 Gy IR.
 - (I) Aggregate plot for ssDNA bound by RAD51 as measured by ChIP-seq at AslSI sites, separated into sense and antisense strands. WT, *BRCA1*^{Δ11}, and *BRCA1*^{Δ11}*53BP1*^{S25A} MEFs (top panels) are compared with their respective counterparts expressing FHA-PALB2 (bottom panels).
- In (A), (D), (E), and (H), a minimum of 300 nuclei per condition were quantified using Gen5 spot analysis software. In (C), a minimum of 130 nuclei per condition were quantified. A representative experiment (n = 2) is shown. Statistical significance was determined by the Mann-Whitney t test in all of the indicated panels.

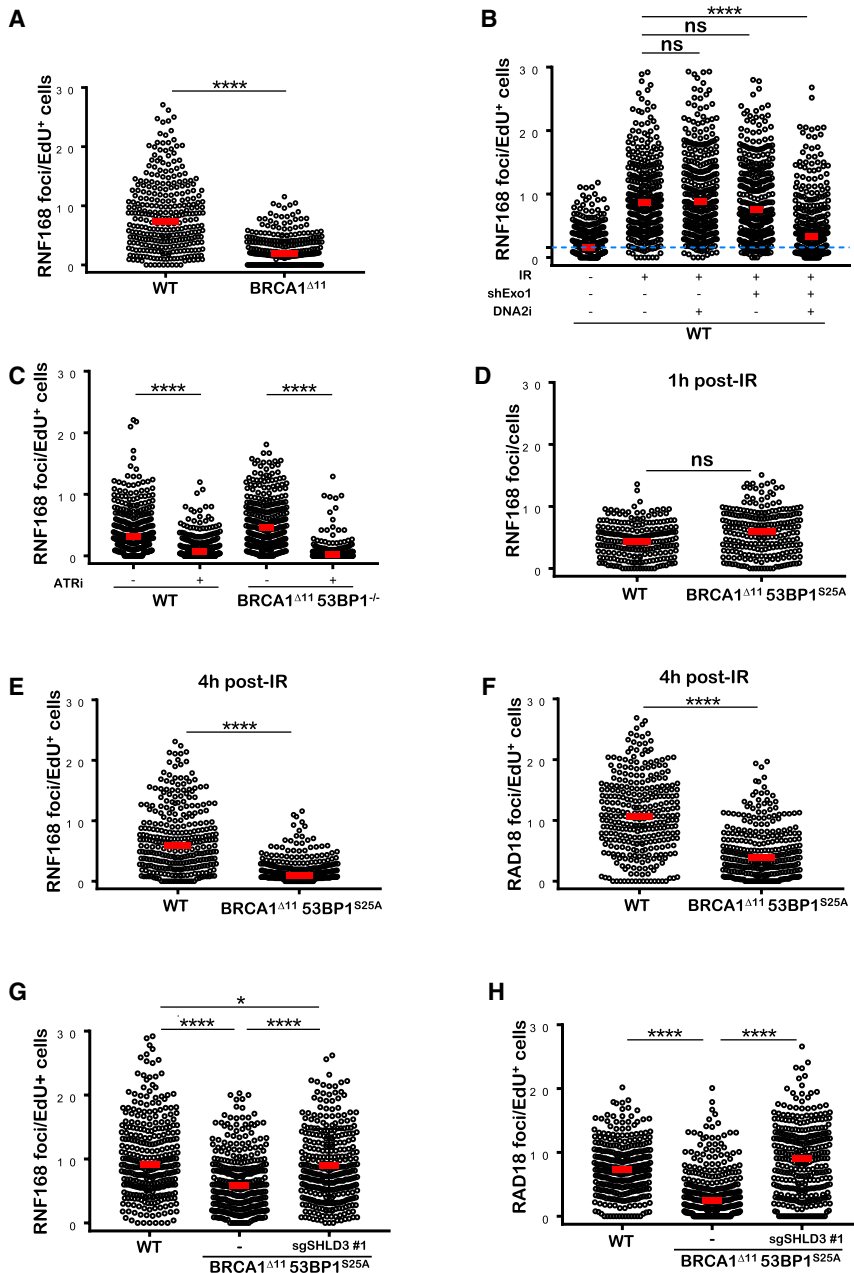


Figure 6. Shieldin Blocks RNF168 Recruitment Post-resection in *BRCA1*^{Δ11}53BP1^{S25A} Cells

(A) Quantification of RNF168 foci in individual EdU-positive nuclei from WT and *BRCA1*^{Δ11} MEFs. Cells were irradiated with 5 Gy and analyzed 4 h post-IR.

(B) Quantification of RNF168 foci in individual EdU-positive nuclei from WT and EXO1-depleted MEFs, pretreated or not with DNA2i (1 μM). Cells were either unirradiated or irradiated with 10 Gy and analyzed 4 h post-IR.

(C) Quantification of RNF168 foci in individual EdU-positive nuclei from WT and *BRCA1*^{Δ11}53BP1^{-/-} MEFs pretreated with ATRi (AZ20, 10 μM). Cells were either unirradiated or irradiated with 10 Gy and analyzed 4 h post-IR.

(D) Quantification of RNF168 foci in WT and *BRCA1*^{Δ11}53BP1^{S25A} MEFs 1 h after 10 Gy IR. Statistical significance was determined by the Wilcoxon rank-sum test.

(E) Quantification of RNF168 foci in individual EdU-positive nuclei from WT and *BRCA1*^{Δ11}53BP1^{S25A} MEFs 4 h post-IR (5 Gy). Statistical significance was determined by the Wilcoxon rank-sum test.

(F) Quantification of RAD18 foci in individual EdU-positive nuclei from WT and *BRCA1*^{Δ11}53BP1^{S25A} MEFs. Cells were irradiated with 5 Gy and analyzed 4 h post-IR.

(G) Quantification of RNF168 foci in individual EdU-positive nuclei from WT, *BRCA1*^{Δ11}53BP1^{S25A}, and *BRCA1*^{Δ11}53BP1^{S25A}SHLD3^{-/-} MEFs. Cells were irradiated with 5 Gy and analyzed 4 h post-IR.

(H) Quantification of RAD18 foci in individual EdU-positive nuclei from WT, *BRCA1*^{Δ11}53BP1^{S25A} MEFs, and *BRCA1*^{Δ11}53BP1^{S25A}SHLD3^{-/-} MEFs. Cells were irradiated with 5 Gy and analyzed 4 h post-IR.

In (A)–(H), a minimum of 300 nuclei per condition were quantified using Gen5 spot analysis software. A representative experiment ($n = 2$) is shown. Unless otherwise noted, statistical significance was determined by the Mann-Whitney t test in all of the panels.

of RIF1/shieldin activity, can be overcome by forced PALB2 loading to chromatin (Figures 5E–5H) in a manner dependent on the interaction of PALB2 with BRCA2 (Figures S5F and S5G). In *BRCA1*-deficient cells, the recruitment of PALB2/BRCA2 to ssDNA is dependent on RNF168-driven H2A-K15 ubiquitylation (Zong et al., 2019). Our data thus suggest that shieldin binding to resected ends can directly compete with RNF168, leading to defective PALB2 accrual, which prevents the nucleation of RAD51 filaments (Figure S6). However, a more direct role of shieldin in antagonizing BRCA2 activity cannot be discounted.

The post-resection anti-recombination functions of 53BP1 described herein may be relevant to the mechanism of chemo-

therapy resistance in a subset of *BRCA1*-mutated tumors. Germline pathogenic mutations in the RING domain, exemplified by the 185delAG founder mutation commonly found in the Ashkenazi Jewish population, are associated with breast and ovarian cancers and predict poor responses to chemotherapy (Drost et al., 2016; Wang et al., 2016). Therapy resistance in this setting has been linked to the overexpression of the hypomorphic RING-less BRCA1 protein, and is associated with partially recovered RAD51 loading and HR (Drost et al., 2016; Wang et al., 2016). By contrast, we found that non-cancerous cells expressing RING-less BRCA1 at physiological levels, despite robust end resection, are highly defective in RAD51 loading (Figures 7), which can be corrected by the

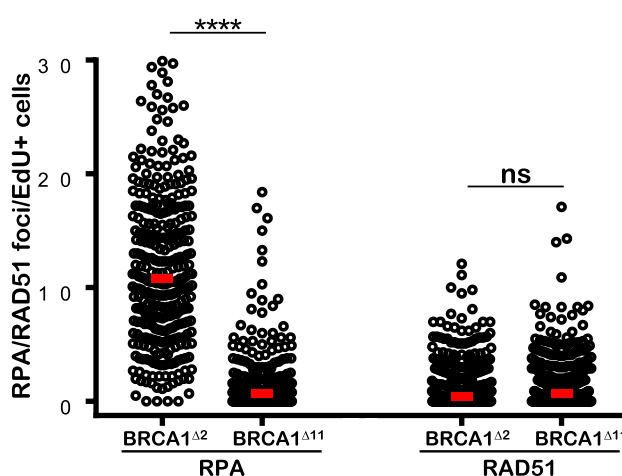


Figure 7. RING-less BRCA1 Supports End Resection but Not RAD51 Filament Assembly

Left: IR-induced RPA foci per EdU-positive nuclei in *BRCA1*^{F2/F2} MEFs with adenoviral Cre infection, which deletes *BRCA1* exon 2 (*BRCA2*^{Δ2}), and in *BRCA1*^{Δ11} cells. Right: IR-induced RAD51 foci per EdU-positive nucleus in *BRCA2*^{Δ2} and *BRCA1*^{Δ11} cells.

A minimum of 300 nuclei per condition were quantified using Gen5 spot analysis software. A representative experiment ($n = 2$) is shown. Statistical significance was determined by the Mann-Whitney t test.

loss of 53BP1 (Zong et al., 2019). We therefore propose that when the RING-less BRCA1 is overexpressed in cancers, its residual hypomorphic activity is able to partially overcome 53BP1/shieldin binding to resected DNA ends, leading to the partial restoration of HR and the development of chemotherapy resistance.

In summary, the expression of 53BP1^{S25A} on a *BRCA1* mutant background produces a striking uncoupling of end resection from downstream RAD51 loading and suggests that embryonic viability requires end resection but not necessarily efficient HR. These data support a model in which 53BP1 antagonizes two key steps in HR that are normally mediated by BRCA1.

STAR★METHODS

Detailed methods are provided in the online version of this paper and include the following:

- KEY RESOURCES TABLE
- LEAD CONTACT AND MATERIALS AVAILABILITY
- EXPERIMENTAL MODEL AND SUBJECT DETAILS
- METHOD DETAILS
 - MEFs generation
 - Plasmids and transfection
 - Immunoblotting and Immunofluorescence
 - Metaphase spreads, clonogenic survival and viability assays
 - Single Strand Annealing (SSA) assay
 - Purification of TAP-53BP1 complex and MS/MS analysis
 - *In vivo* PARP inhibitor treatment and histopathological analyses

- Magnetic Resonance and X-Ray imaging
- END-seq and ChIP-SSDS
- Statistical analyses

● DATA AND CODE AVAILABILITY

SUPPLEMENTAL INFORMATION

Supplemental Information can be found online at <https://doi.org/10.1016/j.molcel.2019.09.024>.

ACKNOWLEDGMENTS

We thank Anthony Tubbs for comments on the paper; Jennifer Mehalko and Dom Esposito (Protein Expression Laboratory, Frederick National Laboratory for Cancer Research) for transgenic constructs; Karim Bakhtiar, Diana Haines, and Elijah Edmonson (Pathology/Histotechnology Laboratory, Frederick National Laboratory for Cancer Research) for rodent necropsy, pathology analysis, and imaging; Joseph Kalen and Nimit Patel (Small Animal Imaging Program, Frederick National Laboratory for Cancer Research) for X-ray computed tomography (CT) scan imaging; Jennifer Wise and Kelly Smith for assistance with animal work; Davide Robbiani and Kai Ge for antibodies; Dan Durocher for shieldin constructs; David Goldstein and the CCR Genomics core for sequencing support; and Neil Johnson for discussions. Research in the J.M.S. laboratory is supported by NIH grant R01CA197506. Research in the N.M. laboratory is supported by NIH grant R01 227001. The A.N. laboratory is supported by the Intramural Research Program of the NIH, an Ellison Medical Foundation Senior Scholar in Aging Award (AG-SS- 2633-11), the Department of Defense Idea Expansion (W81XWH-15-2-006) and Breakthrough (W81XWH-16-1-599) Awards, the Alex's Lemonade Stand Foundation Award, and an NIH Intramural FLEX Award.

AUTHOR CONTRIBUTIONS

E.C., D.Z., N.W., A.S., M.I., R.P., L.C.D., A.K.B., C.M.-D., P.M., A.D., and M.J.K. designed and performed experiments; W.W. and Y.M. analyzed the data; A.C., M.A.B., J.M.S., N.M., P.J.M., and A.N. supervised and provided advice; E.C., D.Z., and A.N. wrote the manuscript with comments from the authors.

DECLARATION OF INTERESTS

The authors declare no competing interests.

Received: June 24, 2019

Revised: August 17, 2019

Accepted: September 20, 2019

Published: October 22, 2019

REFERENCES

- Alver, R.C., Chadha, G.S., Gillespie, P.J., and Blow, J.J. (2017). Reversal of DDK-Mediated MCM Phosphorylation by Rif1-PP1 Regulates Replication Initiation and Replisome Stability Independently of ATR/Chk1. *Cell Rep.* 18, 2508–2520.
- Ameziane, N., May, P., Haitjema, A., van de Vrugt, H.J., van Rossum-Fikkert, S.E., Ristic, D., Williams, G.J., Balk, J., Rockx, D., Li, H., et al. (2015). A novel Fanconi anaemia subtype associated with a dominant-negative mutation in RAD51. *Nat. Commun.* 6, 8829.
- Aymard, F., Bugler, B., Schmidt, C.K., Guillou, E., Caron, P., Briois, S., Iacovoni, J.S., Daburon, V., Miller, K.M., Jackson, S.P., and Legube, G. (2014). Transcriptionally active chromatin recruits homologous recombination at DNA double-strand breaks. *Nat. Struct. Mol. Biol.* 21, 366–374.
- Baer, R., and Ludwig, T. (2002). The BRCA1/BARD1 heterodimer, a tumor suppressor complex with ubiquitin E3 ligase activity. *Curr. Opin. Genet. Dev.* 12, 86–91.

- Bouwman, P., Aly, A., Escandell, J.M., Pieterse, M., Bartkova, J., van der Gulden, H., Hiddingh, S., Thanasoula, M., Kulkarni, A., Yang, Q., et al. (2010). 53BP1 loss rescues BRCA1 deficiency and is associated with triple-negative and BRCA-mutated breast cancers. *Nat. Struct. Mol. Biol.* 17, 688–695.
- Brick, K., Pratto, F., Sun, C.Y., Camerini-Otero, R.D., and Petukhova, G. (2018). Analysis of Melotic Double-Strand Break Initiation in Mammals. *Methods Enzymol.* 601, 391–418.
- Bunting, S.F., Callén, E., Wong, N., Chen, H.T., Polato, F., Gunn, A., Bothmer, A., Feldhahn, N., Fernandez-Capetillo, O., Cao, L., et al. (2010). 53BP1 inhibits homologous recombination in Brca1-deficient cells by blocking resection of DNA breaks. *Cell* 141, 243–254.
- Buonomo, S.B., Wu, Y., Ferguson, D., and de Lange, T. (2009). Mammalian Rif1 contributes to replication stress survival and homology-directed repair. *J. Cell Biol.* 187, 385–398.
- Callen, E., Di Virgilio, M., Kruhlak, M.J., Nieto-Soler, M., Wong, N., Chen, H.T., Faryabi, R.B., Polato, F., Santos, M., Starnes, L.M., et al. (2013). 53BP1 mediates productive and mutagenic DNA repair through distinct phosphoprotein interactions. *Cell* 153, 1266–1280.
- Canela, A., Sridharan, S., Sciascia, N., Tubbs, A., Meltzer, P., Sleckman, B.P., and Nussenzweig, A. (2016). DNA Breaks and End Resection Measured Genome-wide by End Sequencing. *Mol. Cell* 63, 898–911.
- Canela, A., Maman, Y., Jung, S., Wong, N., Callen, E., Day, A., Kieffer-Kwon, K.R., Pekowska, A., Zhang, H., Rao, S.S.P., et al. (2017). Genome Organization Drives Chromosome Fragility. *Cell* 170, 507–521.e18.
- Cao, L., Xu, X., Bunting, S.F., Liu, J., Wang, R.H., Cao, L.L., Wu, J.J., Peng, T.N., Chen, J., Nussenzweig, A., et al. (2009). A selective requirement for 53BP1 in the biological response to genomic instability induced by Brca1 deficiency. *Mol. Cell* 35, 534–541.
- Chen, C.C., Feng, W., Lim, P.X., Kass, E.M., and Jasin, M. (2018). Homology-Directed Repair and the Role of BRCA1, BRCA2, and Related Proteins in Genome Integrity and Cancer. *Annu. Rev. Cancer Biol.* 2, 313–336.
- Cho, E.A., Prindle, M.J., and Dressler, G.R. (2003). BRCT domain-containing protein PTIP is essential for progression through mitosis. *Mol. Cell. Biol.* 23, 1666–1673.
- Chronis, C., Fiziev, P., Papp, B., Butz, S., Bonora, G., Sabri, S., Ernst, J., and Plath, K. (2017). Cooperative Binding of Transcription Factors Orchestrates Reprogramming. *Cell* 168, 442–459.e20.
- Cuella-Martin, R., Oliveira, C., Lockstone, H.E., Snellenberg, S., Grobmußova, N., and Chapman, J.R. (2016). 53BP1 Integrates DNA Repair and p53-Dependent Cell Fate Decisions via Distinct Mechanisms. *Mol. Cell* 64, 51–64.
- Daniel, J.A., Santos, M.A., Wang, Z., Zang, C., Schwab, K.R., Jankovic, M., Filsuf, D., Chen, H.T., Gazumyan, A., Yamane, A., et al. (2010). PTIP promotes chromatin changes critical for immunoglobulin class switch recombination. *Science* 329, 917–923.
- Dev, H., Chiang, T.W., Lescale, C., de Krijger, I., Martin, A.G., Pilger, D., Coates, J., Sczaniecka-Clift, M., Wei, W., Ostermaier, M., et al. (2018). Shieldin complex promotes DNA end-joining and counters homologous recombination in BRCA1-null cells. *Nat. Cell Biol.* 20, 954–965.
- Doil, C., Mailand, N., Bekker-Jensen, S., Menard, P., Larsen, D.H., Pepperkok, R., Ellenberg, J., Panier, S., Durocher, D., Bartek, J., et al. (2009). RNF168 binds and amplifies ubiquitin conjugates on damaged chromosomes to allow accumulation of repair proteins. *Cell* 136, 435–446.
- Drost, R., Dhillon, K.K., van der Gulden, H., van der Heijden, I., Brandsma, I., Cruz, C., Chondronasiou, D., Castroviejo-Bermejo, M., Boon, U., Schut, E., et al. (2016). BRCA1185delAG tumors may acquire therapy resistance through expression of RING-less BRCA1. *J. Clin. Invest.* 126, 2903–2918.
- Eng, J.K., McCormack, A.L., and Yates, J.R. (1994). An approach to correlate tandem mass spectral data of peptides with amino acid sequences in a protein database. *J. Am. Soc. Mass Spectrom.* 5, 976–989.
- Findlay, S., Heath, J., Luo, V.M., Malina, A., Morin, T., Coulombe, Y., Djerir, B., Li, Z., Samiei, A., Simo-Cheyrou, E., et al. (2018). SHLD2/FAM35A co-operates with REV7 to coordinate DNA double-strand break repair pathway choice. *EMBO J.* 37, e100158.
- Gao, S., Feng, S., Ning, S., Liu, J., Zhao, H., Xu, Y., Shang, J., Li, K., Li, Q., Guo, R., and Xu, D. (2018). An OB-fold complex controls the repair pathways for DNA double-strand breaks. *Nat. Commun.* 9, 3925.
- Ghezraoui, H., Oliveira, C., Becker, J.R., Bilham, K., Moralli, D., Anzilotti, C., Fischer, R., Deobagkar-Lele, M., Sanchez-Calvo, M., Fueyo-Marcos, E., et al. (2018). 53BP1 cooperation with the REV7-shieldin complex underpins DNA structure-specific NHEJ. *Nature* 560, 122–127.
- Gong, Z., Cho, Y.W., Kim, J.E., Ge, K., and Chen, J. (2009). Accumulation of Pax2 transactivation domain interaction protein (PTIP) at sites of DNA breaks via RNF8-dependent pathway is required for cell survival after DNA damage. *J. Biol. Chem.* 284, 7284–7293.
- Gupta, R., Somyajit, K., Narita, T., Maskey, E., Stanlie, A., Kremer, M., Typas, D., Lammers, M., Mailand, N., Nussenzweig, A., et al. (2018). DNA Repair Network Analysis Reveals Shieldin as a Key Regulator of NHEJ and PARP Inhibitor Sensitivity. *Cell* 173, 972–988.e23.
- Hu, Q., Botuyan, M.V., Cui, G., Zhao, D., and Mer, G. (2017). Mechanisms of Ubiquitin-Nucleosome Recognition and Regulation of 53BP1 Chromatin Recruitment by RNF168/169 and RAD18. *Mol. Cell* 66, 473–487.e9.
- Huang, J., Huen, M.S., Kim, H., Leung, C.C., Glover, J.N., Yu, X., and Chen, J. (2009). RAD18 transmits DNA damage signalling to elicit homologous recombination repair. *Nat. Cell Biol.* 11, 592–603.
- Karolchik, D., Hinrichs, A.S., Furey, T.S., Roskin, K.M., Sugnet, C.W., Haussler, D., and Kent, W.J. (2004). The UCSC Table Browser data retrieval tool. *Nucleic Acids Res.* 32, D493–D496.
- Kent, W.J., Sugnet, C.W., Furey, T.S., Roskin, K.M., Pringle, T.H., Zahler, A.M., and Haussler, D. (2002). The human genome browser at UCSC. *Genome Res.* 12, 996–1006.
- Kowalczykowski, S.C. (2015). An Overview of the Molecular Mechanisms of Recombinational DNA Repair. *Cold Spring Harb. Perspect. Biol.* 7, a016410.
- Langmead, B., Trapnell, C., Pop, M., and Salzberg, S.L. (2009). Ultrafast and memory-efficient alignment of short DNA sequences to the human genome. *Genome Biol.* 10, R25.
- Li, M., Cole, F., Patel, D.S., Misenko, S.M., Her, J., Malhowski, A., Alhamza, A., Zheng, H., Baer, R., Ludwig, T., et al. (2016). 53BP1 ablation rescues genomic instability in mice expressing ‘RING-less’ BRCA1. *EMBO Rep.* 17, 1532–1541.
- Ludwig, T., Chapman, D.L., Papaioannou, V.E., and Efstratiadis, A. (1997). Targeted mutations of breast cancer susceptibility gene homologs in mice: lethal phenotypes of Brca1, Brca2, Brca1/Brca2, Brca1/p53, and Brca2/p53 nullizygous embryos. *Genes Dev.* 11, 1226–1241.
- Mirman, Z., Lottersberger, F., Takai, H., Kibe, T., Gong, Y., Takai, K., Bianchi, A., Zimmermann, M., Durocher, D., and de Lange, T. (2018). 53BP1-RIF1-shieldin counteracts DSB resection through CST- and Pol γ -dependent fill-in. *Nature* 560, 112–116.
- Nakatani, Y., and Ogryzko, V. (2003). Immunoaffinity purification of mammalian protein complexes. *Methods Enzymol.* 370, 430–444.
- Niedernhofer, L.J., Gurkar, A.U., Wang, Y., Vijg, J., Hoeijmakers, J.H.J., and Robbins, P.D. (2018). Nuclear Genomic Instability and Aging. *Annu. Rev. Biochem.* 87, 295–322.
- Noordermeer, S.M., Adam, S., Setiaputra, D., Barazas, M., Pettitt, S.J., Ling, A.K., Olivier, M., Álvarez-Quilón, A., Moatti, N., Zimmermann, M., et al. (2018). The shieldin complex mediates 53BP1-dependent DNA repair. *Nature* 560, 117–121.
- Orthwein, A., Noordermeer, S.M., Wilson, M.D., Landry, S., Enchev, R.I., Sherker, A., Munro, M., Pinder, J., Salsman, J., Dellaire, G., et al. (2015). A mechanism for the suppression of homologous recombination in G1 cells. *Nature* 528, 422–426.
- Panier, S., Ichijima, Y., Fradet-Turcotte, A., Leung, C.C., Kaustov, L., Arrowsmith, C.H., and Durocher, D. (2012). Tandem protein interaction modules organize the ubiquitin-dependent response to DNA double-strand breaks. *Mol. Cell* 47, 383–395.

- Quinlan, A.R., and Hall, I.M. (2010). BEDTools: a flexible suite of utilities for comparing genomic features. *Bioinformatics* 26, 841–842.
- Ray Chaudhuri, A., Callen, E., Ding, X., Gogola, E., Duarte, A.A., Lee, J.E., Wong, N., Lafarga, V., Calvo, J.A., Panzarino, N.J., et al. (2016). Replication fork stability confers chemoresistance in BRCA-deficient cells. *Nature* 535, 382–387.
- R Development Core Team (2008). R: A language and environment for statistical computing (R Foundation for Statistical Computing).
- Setiaputra, D., and Durocher, D. (2019). Shieldin - the protector of DNA ends. *EMBO Rep.* 20, e47560.
- Stark, J.M., Pierce, A.J., Oh, J., Pastink, A., and Jasin, M. (2004). Genetic steps of mammalian homologous repair with distinct mutagenic consequences. *Mol. Cell. Biol.* 24, 9305–9316.
- Stewart, G.S., Panier, S., Townsend, K., Al-Hakim, A.K., Kolas, N.K., Miller, E.S., Nakada, S., Ylanko, J., Olivarius, S., Mendez, M., et al. (2009). The RIDDLE syndrome protein mediates a ubiquitin-dependent signaling cascade at sites of DNA damage. *Cell* 136, 420–434.
- Symington, L.S. (2016). Mechanism and regulation of DNA end resection in eukaryotes. *Crit. Rev. Biochem. Mol. Biol.* 51, 195–212.
- Takenaka, S., Kuroda, Y., Ohta, S., Mizuno, Y., Hiwatari, M., Miyatake, S., Matsumoto, N., and Oka, A. (2019). A Japanese patient with RAD51-associated Fanconi anemia. *Am. J. Med. Genet. A* 179, 900–902.
- Turner, J.M., Mahadevaiah, S.K., Fernandez-Capetillo, O., Nussenzweig, A., Xu, X., Deng, C.X., and Burgoyne, P.S. (2005). Silencing of unsynapsed meiotic chromosomes in the mouse. *Nat. Genet.* 37, 41–47.
- Wang, A.T., Kim, T., Wagner, J.E., Conti, B.A., Lach, F.P., Huang, A.L., Molina, H., Sanborn, E.M., Zierhut, H., Cornes, B.K., et al. (2015). A Dominant Mutation in Human RAD51 Reveals Its Function in DNA Interstrand Crosslink Repair Independent of Homologous Recombination. *Mol. Cell* 59, 478–490.
- Wang, Y., Bernhardy, A.J., Cruz, C., Krais, J.J., Nacson, J., Nicolas, E., Peri, S., van der Gulden, H., van der Heijden, I., O'Brien, S.W., et al.; KConFab Investigators (2016). The BRCA1-Δ11q Alternative Splice Isoform Bypasses Germline Mutations and Promotes Therapeutic Resistance to PARP Inhibition and Cisplatin. *Cancer Res.* 76, 2778–2790.
- Ward, I.M., Minn, K., van Deursen, J., and Chen, J. (2003). p53 Binding protein 53BP1 is required for DNA damage responses and tumor suppression in mice. *Mol. Cell. Biol.* 23, 2556–2563.
- Zhang, Y., Liu, T., Meyer, C.A., Eeckhoute, J., Johnson, D.S., Bernstein, B.E., Nusbaum, C., Myers, R.M., Brown, M., Li, W., and Liu, X.S. (2008). Model-based analysis of ChIP-Seq (MACS). *Genome Biol.* 9, R137.
- Zhou, Y., Caron, P., Legube, G., and Paull, T.T. (2014). Quantitation of DNA double-strand break resection intermediates in human cells. *Nucleic Acids Res.* 42, e19.
- Zong, D., Callén, E., Pegoraro, G., Lukas, C., Lukas, J., and Nussenzweig, A. (2015). Ectopic expression of RNF168 and 53BP1 increases mutagenic but not physiological non-homologous end joining. *Nucleic Acids Res.* 43, 4950–4961.
- Zong, D., Adam, S., Wang, Y., Sasanuma, H., Callen, E., Murga, M., Day, A., Kruhlak, M.J., Wong, N., Munro, M., et al. (2019). BRCA1 Haploinsufficiency Is Masked by RNF168-Mediated Chromatin Ubiquitylation. *Mol. Cell* 73, 1267–1281.e7.

STAR★METHODS**KEY RESOURCES TABLE**

REAGENT or RESOURCE	SOURCE	IDENTIFIER
Antibodies		
Rabbit polyclonal anti-53BP1	Novus Biologicals	Cat# NB100-305; RRID: AB_10001695
Rabbit polyclonal anti-53BP1 (phoshro S25)	Abcam	Cat# ab70323; RRID:AB_1267592
Mouse monoclonal anti- α -Tubulin	Sigma-Aldrich	Cat# T-5168; RRID: AB_477579
Rabbit polyclonal anti-Phospho-p53 (Ser15)	Cell Signaling	Cat# 9284; RRID:AB_331464
Mouse monoclonal anti-Chk2	Millipore	Cat# 05-649; RRID:AB_2244941
Mouse monoclonal anti-GFP	Roche Applied Science	Cat# 11814460001; RRID: AB_390913
Rabbit polyclonal anti-Rad51	Abcam	Cat# ab176458; RRID:AB_2665405
Rabbit polyclonal anti-RPA32/RPA2	Abcam	Cat# ab10359; RRID:AB_297095
Rabbit polyclonal anti-RPA32/RPA2	Abcam	Cat# ab76420; RRID:AB_1524336
Sheep polyclonal anti-RNF168	R&D System	Cat# AF7217; RRID:AB_10971653
Mouse monoclonal anti-RAD18	Millipore	Cat# ABE1377
Mouse monoclonal anti-FLAG (M2)	Sigma-Aldrich	Cat# F1804; RRID: AB_262044
Rabbit polyclonal anti-RIF1	Gift from Davide Robbiani	N/A
Mouse monoclonal anti-H2AX (pS139)	N/A	Cat# 05-636; RRID:AB_309864
Guinea pig polyclonal antibody anti-Tbr1	Synaptic Systems	Cat# 328 005; RRID:AB_2620072
Rabbit polyclonal antibody anti-Kap1 (Ser 824)	Bethyl	Cat# A300-767A; RRID:AB_669740
IRDye 680RD Goat anti-Mouse IgG (H+L)	LI-COR Biosciences	Cat# 926-68070; RRID:AB_10956588
IRDye 800CW Goat anti-Rabbit IgG (H+L)	LI-COR Biosciences	Cat# 925-32211; RRID:AB_2651127
FITC-Goat anti-Guinea Pig IgG(H+L)	Jackson ImmunoResearch	Cat# 106-096-003; RRID:AB_2337418
Cy3-Goat anti-Rabbit IgG(H+L)	Jackson ImmunoResearch	Cat# 111-166-003; RRID:AB_2338007
Alexa Fluor 488 Goat anti-Mouse IgG (H+L)	Thermo Fisher Scientific	Cat# A-11001; RRID:AB_2534069
Alexa Fluor 568 Goat anti-Mouse IgG (H+L)	Thermo Fisher Scientific	Cat# A-11031; RRID:AB_144696
Alexa Fluor 568 Goat anti-Rat IgG (H+L)	Thermo Fisher Scientific	Cat# A-11077; RRID:AB_2534121
Alexa Fluor 488 Chicken anti-Rabbit IgG (H+L)	Thermo Fisher Scientific	Cat# A21441; RRID:AB_10563745
Alexa Fluor 568 Goat anti-Rabbit IgG (H+L)	Thermo Fisher Scientific	Cat# A-11011; RRID:AB_143157
Alexa Fluor 568 Donkey anti-Sheep IgG (H+L)	Thermo Fisher Scientific	Cat# A21099; RRID:AB_10055702
Purified Rat anti-Mouse CD180 (RP/14)	BD Biosciences	Cat# 552128; RRID:AB_394343
Bacterial and Virus Strains		
Bacteria: TOP10 Chemically Competent <i>E. coli</i>	Thermo Fisher Scientific	Cat# C404006
Retrovirus: pCL-ECO	Addgene	Cat# 12371; RRID:Addgene_12371
Lentivirus: pSpCas9(BB)-2A-Puro (PX459)	Addgene	Cat# 48139; RRID:Addgene_48139
Mammalian expression pCMV-VsVg envelope lentiviral protein	Gift from Katrin F. Chua	N/A
Mammalian expression lentiviral packaging pCMV-dR8.2	Gift from Katrin F. Chua	N/A
Retrovirus: pMX-empty-IRES-GFP-Puro	Jiri Lukas (Zong et al., 2015)	N/A
Retrovirus: pMX-empty(no IRES-GFP)-Puro	Gift from Davide Robbiani	N/A
Retrovirus: pMX-GFP-PALB2-Puro	(Zong et al., 2015)	N/A
Retrovirus: pMX-GFP-FHA(RNF8)-PALB2-Puro	(Zong et al., 2015)	N/A
Mammalian expression: pCBAScel	Addgene	Cat# 26477; RRID:Addgene_26477
Mammalian expression: pEGFP-N1	Jeremy M. Stark	N/A
Adenovirus: Ad5-CMV-eGFP	Addgene	N/A
Adenovirus: Ad5-CMV-Cre-eGFP	Addgene	N/A

(Continued on next page)

Continued

REAGENT or RESOURCE	SOURCE	IDENTIFIER
Chemicals, Peptides, and Recombinant Proteins		
Olaparib	Selleckchem	Cat# AZD2281
ATR inhibitor (AZ20)	Selleckchem	Cat# S7050
DNA2 inhibitor	NIH Developmental Therapeutics Program	Cat# NSC-105808
Bloom inhibitor (ML216)	Sigma-Aldrich	Cat# SML0661
4-Hydroxytamoxifen	Sigma-Aldrich	Cat# H7904
Doxycycline hyclate	Sigma-Aldrich	Cat# D9891
Lipopolysaccharide (LPS) from <i>E. coli</i> O111:B4	Sigma-Aldrich	Cat# L2630
Interleukin 4 (IL-4) from mouse	Sigma-Aldrich	Cat# I1020
CD43 microbeads (Ly-48)	Miltenyi Biotec	Cat# 130-049-801
Protein G Magnetic Beads	Active Motif	Cat# 104502
X-tremeGENE™ 9 DNA Transfection Reagent	Roche Diagnostics	Cat# 6365809001
Lipofectamine 3000	Thermo Fisher Scientific	Cat# L3000015
Hoechst 33342	Thermo Fisher Scientific	Cat# 62249
GeneArt Seamless Cloning Enzyme Mix	Thermo Fisher Scientific	N/A
Zero Blunt™ PCR Cloning Kit	Thermo Fisher Scientific	Cat# K270020
PNA probe for telomeres Cy3-(CCCTAA) ₃	PNA Bio	Cat# F1002
DAPI	Thermo Fisher Scientific	Cat# 62248
EdU	Thermo Fisher Scientific	Cat# A10044
Colcemid	Roche Diagnostics	Cat# 10295892001
cOmplete, Mini Protease inhibitor cocktail	Roche Diagnostics	Cat# 11836153001
Crystal Violet	Sigma-Aldrich	Cat# 0775
Anti-FLAG M2 magnetic beads	Sigma	Cat# M8823; RRID:AB_2637089
Trizol	Invitrogen	Cat# 15596026
Puregene Proteinase K enzyme	QIAGEN	Cat# 158920
Puregene RNase A Solution	QIAGEN	Cat# 158924
T4 DNA Polymerase	NEB	Cat# M0203L
T4 Polynucleotide Kinase	NEB	Cat# M0201L
DNA Polymerase I, Large (Klenow) Fragment	NEB	Cat# M0210L
Exonuclease T (ExoT)	NEB	Cat# M0265L
Exonuclease VII (ExoVII)	NEB	Cat# M0379L
Klenow Fragment (3' → 5' exo-)	NEB	Cat# M0212L
Quick Ligation Kit	NEB	Cat# M2200L
USER enzyme	NEB	Cat# M5505L
KAPA HiFi HotStart ReadyMix (2X)	KAPA Biosystems	Cat# KK2600
MyOne Streptavidin C1 Beads	ThermoFisher	Cat# 650-01
Agencourt AMPure XP beads	Beckman Coulter	Cat# A63881
Dynabeads Protein A	Thermo Fisher Scientific	Cat# 10002D
Critical Commercial Assays		
Click-IT EdU Alexa Fluor 488 Flow Cytometry Assay Kit	Thermo Fisher Scientific	Cat# C10425
Click-IT EdU Alexa Fluor 647 Flow Cytometry Assay Kit	Thermo Fisher Scientific	Cat# C10634
Vector VIP Substrate kit	Vector laboratories	Cat# SK-4600; RRID:AB_2336848
ApopTag Fluorescein Apoptosis detection kit	Chemicon	Cat# S7110
CellTiter-Glo® Luminescent Cell Viability Assay	Promega	Cat# G7571

(Continued on next page)

Continued

REAGENT or RESOURCE	SOURCE	IDENTIFIER
KAPA Library Quantification Kit	Kapa Biosciences	Cat# KK4824
CHEF Mammalian Genomic DNA plug kit	Bio-Rad	Cat# 1703591
Deposited Data		
Raw and analyzed data	This paper	GSE133808
ChIP-seq for H3K27ac, H3K79me2, H3K27me3	(Chronis et al., 2017)	GSE90893
Experimental Models: Cell Lines		
MEF: Wildtype	This paper	N/A
MEF: BRCA1 ^{Δ11}	This paper	N/A
MEF: 53BP1 ^{S25A}	This paper	N/A
MEF: 53BP1 ^{-/-}	(Bunting et al., 2010)	N/A
MEF: BRCA1 ^{Δ11} 53BP1 ^{-/-}	(Bunting et al., 2010)	N/A
MEF: BRCA1 ^{Δ11} 53BP1 ^{S25A}	This paper	N/A
MEF: BRCA1 ^{Δ2}	(Bunting et al., 2010)	N/A
Experimental Models: Organisms/Strains		
Mouse: BRCA1 ^{+/Δ11} . B6/129	NCI mouse repository	Strain # 01XC9
Mouse: 53BP1 ^{+/S25A} , B6/129	This paper	N/A
Mouse: 53BP1 ^{-/-} . B6/129	(Ward et al., 2003)	N/A
Mouse: p53 ^{+/-} . B6/129	Taconic Biosciences	N/A
Mouse: BRCA1 ^{+/Δ2} . B6/129	(Ludwig et al., 1997)	N/A
Oligonucleotides		
Primers for genotyping 53BP1_S25A allele: Forward, 5'-ggagatggctgagaaagtgc; Reverse, 5'-tcccctggaatggataaca	This paper	N/A
sgRNA targeting endogenous mouse Shieldin-3 locus: Sense 5' CACCGGGAAAGTTGGACTC ATCGTA; Sense 5' CACCGGGAAAGTTGG ACTCATCGTA	(Gupta et al., 2018)	N/A
siRNAs targeting endogenous mouse Shieldin-3 locus: Sense 5' GACUGCACAGUAGAUCUCU UGGAGU and Antisense 5' ACUCCAAGAGAU CUACUGUGCAGUC	Invitrogen	N/A
shRNAs targeting endogenous mouse Exo1 locus: Pool of antisense 5'-ATAGAACTAGAC CTACAGAGC, antisense 5' TTATTCCCTCATC TTAGACGGG and antisense 5' ATCCGTCAA ATATGAGAATCG	Dharmacon	N/A
Primers to confirm Exo1 knockdown by RT- PCR: Forward: 5' AGGGGAACAGAACTCC AAGC, Reverse: 5' CCAGGAACCTTGTTC CGTCT	This paper	N/A
Recombinant DNA		
Plasmid: FLAG-PALB2	(Orthwein et al., 2015)	N/A
Plasmid: GFP-PALB2	(Orthwein et al., 2015)	N/A
Software and Algorithms		
ZEN 2 (blue edition)	Zeiss	https://www.zeiss.com/corporate/int/home.html
Gen5 spot analysis	BioTek	https://www.bioteck.com/
Metafer 4	MetaSystems	https://metasystems-international.com/
Prism 8	GraphPad	https://www.graphpad.com/
RStudio	RStudio Team	https://www.rstudio.com/

(Continued on next page)

Continued

REAGENT or RESOURCE	SOURCE	IDENTIFIER
Bowtie 1.1.2	(Langmead et al., 2009)	https://sourceforge.net/projects/bowtie-bio/files/bowtie/1.1.2/
MACS 1.4.3	(Zhang et al., 2008)	https://pypi.org/pypi/MACS/1.4.3
UCSC database	(Karolchik et al., 2004)	https://genome.ucsc.edu
UCSC genome browser	(Kent et al., 2002)	https://genome.ucsc.edu
Bedtools	(Quinlan and Hall, 2010)	https://github.com/arq5x/bedtools2
R 3.3.5	R Development Core Team, 2008	https://www.r-project.org/
Sequest	(Eng et al., 1994)	N/A
OsiriX v5.7	Pixmeo	https://www.osirix-viewer.com/
MIM v6.6.5	MIM Software Inc.	https://www.mimsoftware.com/
FlowJo (10.1)	FlowJo LLC	https://www.flowjo.com/
Other		
BOSC23 retrovirus packaging cells	ATCC	Cat# CRL-11270; RRID: CVCL_4401
293T lentivirus packaging cells	ATCC	Cat# CRL-11268; RRID:CVCL_1926
NuPAGE 4-12% Bis-Tris Protein Gels	ThermoFisher Scientific	Cat# NP0321BOX
Glass Bottom Microwell Dishes	MatTek Corporation	Cat# P35G-1.5-14-C
FluoroBrite DMEM Media	Thermo Fisher Scientific	Cat# A1896701
LSM510 confocal microscope	Zeiss	N/A
Axio Observer Z1 epifluorescence microscope	Zeiss	N/A
IN Cell Analyzer	GE Healthcare	N/A
Odyssey® CLx Imaging System	LI-COR Biosciences	N/A
Lion heart LX automated microscope	BioTek Instruments	N/A
CyAN ADP cytometer	Beckman Coulter	N/A
FACSCalibur	BD Biosciences	N/A
Cytogenetic drying chamber	Thermotron	N/A
LTQ Orbitrap Velos Pro ion-trap mass spectrometer	Thermo Fisher Scientific	N/A
Aperio ScanScope XT	Leica	N/A
Nano Quant Infinite M200 Pro microplate reader	Tecan	N/A
Mark 1 ¹³⁷ Cs irradiator	JL Shepherd	N/A

LEAD CONTACT AND MATERIALS AVAILABILITY

Further information and requests for reagents may be directed to and will be fulfilled by the corresponding author Andre Nussenzweig (andre_nussenzweig@nih.gov).

All unique/stable reagents generated in this study are available from the Lead Contact with a completed Materials Transfer Agreement.

EXPERIMENTAL MODEL AND SUBJECT DETAILS

A targeting construct containing the S25A mutation in murine 53BP1 was constructed by amplification of sequences from BAC clone RP23-179G19 (CHORI, Oakland, CA). Briefly, the left homology arm consisting of 5.1 kB of sequence prior to exon 2 of 53BP1 was inserted into an Entry clone using Gateway recombinational cloning (ThermoFisher, Carlsbad, CA) and flanked by Gateway attB4 and attB1 sites. The right homology arm consisting of exon 2 with an embedded S25A mutation and 3.1 kB of downstream homologous DNA in the subsequent intron was constructed using overlap extension PCR to introduce the appropriate mutation (TCT to GCT) and flanked by Gateway attB2 and attB3 sequences. Homology arm clones were sequenced in their entirety to ensure that no PCR mutations were introduced during amplification. Validated clones were used in a Multisite Gateway recombination reaction along with a selection cassette consisting of an attB1-attB2 flanked reverse orientation PGK promoter-neomycin resistance-BgH polyA fragment and introduced into a Gateway pUC19 destination vector with flanking attR4 and attR3 sites. The final targeting clone consists of the

9.1 kB sequence: left homology arm-(pA-neo-PGK)-exon 2 S25A-right homology arm and is flanked by NotI sites for release of the transgene from the vector backbone. Two derivative targeted ES clones were injected into C57BL/6 blastocysts. The resultant chimeric offspring was backcrossed with wild-type C57BL/6 mice, producing *53BP1^{+/S25A}* animals. Germline transmission of the targeted allele was confirmed by PCR (forward primer: 5' ggagatggctgagaaagtgc 3'; reverse primer: 5' tcccctggaatgaaataaca 3'). The PGK-neo cassette was removed by crossing to β-actin-Cre transgenic mice (Jackson Laboratory). *BRCA1^{+/d11}* mice were obtained from the NCI mouse repository. *53BP1^{-/-}* mice were a gift from Junjie Chen. *p53^{-/-}* mice were obtained from Taconic Biosciences. All mouse breeding and experimentation followed protocols approved by the National Institutes of Health Institutional Animal Care and Use Committee.

METHOD DETAILS

MEFs generation

Mouse embryonic fibroblasts (MEFs) were generated from E13.5 embryos and grown in Dulbecco's Modified Eagle's Medium (DMEM, GIBCO) supplemented with 15% heat-inactivated fetal bovine serum (FBS, Gemini Bio-Products) and 1% penicillin + streptomycin (GIBCO). To establish immortalized MEF cell lines, primary MEFs between passages 2-4 were transiently transfected with a vector encoding SV40 T-antigen (pCMV-SV40T). SV40-immortalized MEFs were routinely cultured in DMEM supplemented with 10 or 15% FBS.

For knockdown of Shieldin-3 in MEFs, CRISPR/Cas9 technology was used by cloning the gene-specific gRNAs into pX459 vector (Sense 5' CACCGGGAGTTGGACTCATCGTA 3' and Antisense 5' AAACTACGATGAGTCCAACTTCCC 3') as described (Gupta et al., 2018). Cells were transfected with Lipofectamine following manufacturer's procedure, selected with puromycin for 48 hours and subjected to single clone isolation. Confirmation of the mutated loci was done through PCR amplification and sequencing of the targeted region.

For transient depletion of endogenous Shieldin-3, siRNA technology (Invitrogen) was used (Sense 5' GACUGCACAGUAGAUUCUUGGAGU 3' and Antisense 5' ACUCCAAGAGAUUCUACUGUGCAGUC 3'). siRNA was transfected with Lipofectamine RNAiMAX (Invitrogen) as per manufacturer's instructions.

For knockdown of EXO1, a pool of TRC lentiviral short hairpins were used (Dharmacon. 71124 antisense 5' ATAGAACTAGACC TACAGAGC 3', 71126 antisense 5' TTATTCCTCATCTTAGACGGG 3' and 71127 antisense 5' ATCCGTCAAATATGAGAATCG 3'). Lentiviral particles were produced by transfecting 293T cells with Lipofectamine-3000 as per manufacturer's instructions. Forty-eight hours later, viral supernatant was harvested and used to transduce MEFs. Cells were selected with puromycin and used two days later. EXO1 knockdown was confirmed by RT-PCR using the following primers: Forward: 5' AGGGGAACAGAACTCCAAGC 3', Reverse2: 5' CCAGGAACCTGTTCCGTCT 3'. Samples were run and analyzed on a BioRad CFX96 Real-Time PCR detection system. For microirradiation, MEFs were presensitized in DMEM media containing 0.1 µg/ml of Hoechst 33342 for 60 min before replacing it with phenol red free media containing 5 mM HEPES, and then irradiated with the 364-nm laser line on a LSM510 confocal microscope (Carl Zeiss, Inc.) equipped with a heated stage. Cells were allowed to recover for 1 hour before processing for immunofluorescence.

Plasmids and transfection

Retroviral pMX-PIE-based vectors encoding fusion protein of EGFP-FHA-PALB2(del)s were produced as follows: cDNAs corresponding to truncated human PALB2 proteins were produced by PCR amplification from either pDEST-FRT-TO-GFP-PALB2 1-103, -PALB2-deltaCHAM, -PALB2-deltaMRG15, or -PALB2-deltaWD40 (gifts from Dr. Daniel Durocher) then ligated with cDNA corresponding to FHA domain of human RNF8 fused with EGFP (Zong et al., 2019). The resulting EGFP-FHA-PALB2(del) fragments were subcloned into pMX-PIE vector at the multi-cloning site (MluI/PacI). Infection-competent retroviral particles were assembled in BOSC23 cells co-transfected with the pCL-ECO helper virus. Retroviral supernatant was collected 40–48 h later to transduce MEFs

Immunoblotting and Immunofluorescence

Western blotting was performed as described previously (Zong et al., 2019). Briefly, cells were collected and lysed in a buffer containing 50 mM Tris-HCl (pH 7.5), 200 mM NaCl, 5% Tween-20, 0.5% NP-40, 2 mM PMSF, 2.5 mM β-glycerophosphate (all from Sigma-Aldrich) and protease inhibitor cocktail tablet (complete Mini, Roche Diagnostics). Equal amounts of protein were loaded into precast mini-gels (Invitrogen) and resolved by SDS-PAGE. Proteins were blotted onto a nitrocellulose membrane, blocked with 5% membrane blocking agent (GE Healthcare) in TBS and incubated with the corresponding primary antibody. Primary antibodies were used at the following dilutions: anti-53BP1 (1:1000, Novus Biologicals), anti-phospho53BP1-S25 (1:500, Abcam), anti-Tubulin (1:10,000, Sigma-Aldrich), anti-phospho-53(S15) (1:500, Cell Signaling), anti-Chk2 (1:1500, Upstate Biotechnology). Fluorescent secondary antibodies were used at a dilution of 1:15,000 (Li-Cor Biosciences). Detection of protein bands was performed by fluorescence imaging using a Li-Cor Odyssey CLx imaging system (Li-Cor Biosciences).

For immunofluorescence staining, MEFs were grown on 18 mm x 18 mm glass coverslips, and B lymphocytes were attached to slides coated with CellTak (BD Biosciences). Prior to γ-irradiation (¹³⁷Cs Mark 1 irradiator, JL Shepherd), cells were incubated with 10 µM EdU (Invitrogen) for 20 min. Where indicated, cells were additionally pretreated with 1 µM NSC-105808 (DNA2i) or 10 µM AZ20 (ATRi) for 1 hour. Following irradiation, cells were allowed to recover for 1 hour or 4 hours. Pre-extraction and fixation of samples were

carried out as previously described (Zong et al., 2019). The antibodies used for standard immunofluorescence experiments were anti-RIF1 (1:5,000, gift of Davide Robbiani, Rockefeller University), anti-53BP1 (1:1000, Novus), anti-RAD51 (1:250, Abcam), anti-RPA (1:5,000, Abcam), anti-RNF168 (1:100, R&D Systems), anti-RAD18 (1:5000, Millipore), anti-GFP (1:500, Roche). For laser microirradiation experiments, primary antibodies were anti- γ H2AX (1:5000, Upstate Biotechnology) and anti-PTIP (1 μ g/ml, gift of Kai Ge). Detection was achieved using fluorochrome-conjugated secondary antibodies (Invitrogen). Where indicated, Click-IT chemistry was performed as per manufacturer's instructions (Thermo Fisher Scientific). Finally, DNA was counterstained with DAPI (Thermo Fisher Scientific). Images were captured at 63 \times magnification with an AxioCam MRC5 attached to an Axio Observer Z1 epifluorescence microscope (Zeiss) or at 40 \times magnification on a Lionheart LX automated microscope (BioTek Instruments, Inc.). Quantification of nuclear foci and total nuclear intensity was performed using the Gen5 spot analysis software (BioTek). ZEN Blue (Zeiss) was used to quantify fluorescence intensities of laser stripes.

Metaphase spreads, clonogenic survival and viability assays

Activated asynchronous B cells and MEFs were treated with 1 μ M PARPi (AZD2281, Selleckchem) for 16 hours, subsequently arrested at mitosis with 0.1 μ g/ml colcemid (Roche) and metaphase chromosome spreads were prepared as previously described (Zong et al., 2019). Images were acquired using a Metafer automated scanning and imaging platform (MetaSystems).

To assay for clonogenic survival, MEFs were seeded in 6 cm dishes and treated continuously with 1 μ M PARPi (Selleckchem) or exposed to the indicated doses of IR. After 9 days, culture dishes were stained with 0.5% crystal violet. Colonies containing >50 cells were counted. Clonogenic survival for a given treatment was calculated relative to the plating efficiency in non-treated controls.

To determine cell growth and viability, MEFs were plated in 6-well plates (10,000 per well) and treated continuously with different doses of PARPi for 10 days. The drug-containing medium was replenished every three days and cells were subcultured when they approach confluence. On day 10, cell viability was determined using the CellTiter-Glo Luminescent Cell Viability Assay (Promega) as per manufacturer's instructions.

Single Strand Annealing (SSA) assay

To measure SSA, MEFs resuspended in 800 μ l of OptiMEM were electroporated with 15 μ g of linearized SA-GFP reporter (Stark et al., 2004). Cells were selected in puromycin, and puromycin-resistant clones were pooled for analysis. The pools of clones were seeded onto a 24 well dish at 5–7 \times 10⁵ cells per well, transfected the next day with 0.5 μ g of I-SceI expression plasmid (pCBASce) or GFP expression plasmid with 1.8 μ l Lipofectamine 2000 (Thermo Fisher Scientific) overnight. GFP⁺ cells were analyzed three days after the start of transfection, using a CyAN ADP cytometer (Beckman Coulter). Repair frequencies were normalized to transfection efficiency, using the parallel transfections with the GFP expression vector.

Purification of TAP-53BP1 complex and MS/MS analysis

Purification of 53BP1 was performed using an established tandem immunoaffinity method (Nakatani and Ogryzko, 2003). Flag-HA-53BP1 was stably expressed after transduction of pOZ-Flag-HA-53BP1 retrovirus into HeLa-S cells. Cells were harvested and resuspended in 5X volume of hypotonic buffer (10 mM Tris, pH 7.3, 10 mM KCl, 1.5 mM MgCl₂, 0.2 mM PMSF, 10 mM β -mercaptoethanol, and protease inhibitors (Pierce)). Cells were pelleted by spinning at 2,500 rpm, resuspended in 1X pellet volume of hypotonic buffer and homogenized using a dounce tissue grinder (Wheaton). Nuclear material was pelleted, resuspended in 0.5X pellet volume of low salt buffer (20 mM Tris pH 7.3, 20 mM KCl, 1.5 mM MgCl₂, 0.2 mM EDTA, 25% glycerol, 0.2 mM PMSF, 10 mM β -mercaptoethanol, and protease inhibitors), and dounced again. 0.5X pellet volume of high salt buffer (20 mM Tris pH 7.3, 1.2M KCl, 1.5 mM MgCl₂, 0.2 mM EDTA, 25% glycerol, 0.2 mM PMSF, 10 mM β -mercaptoethanol, and protease inhibitors) was slowly added to nuclear extract, which was subsequently stirred for 30–45 minutes. Extract was spun down at 14,000 rpm for 30 minutes and the soluble material was dialyzed in BC100 buffer (20 mM Tris pH 7.3, 100 mM KCl, 0.2 mM EDTA, 20% Glycerol, 0.2 mM PMSF, 1 mM β -mercaptoethanol). 53BP1 complex was purified from the nuclear extract using anti-Flag (M2) resin (Sigma), followed by purification using anti-HA (F-7) resin (Santa Cruz) in TAP buffer (50 mM Tris-HCl pH 7.9, 100 mM KCl, 5 mM MgCl₂, 10% glycerol, 0.1% NP-40, 1 mM DTT, and protease inhibitors). For both Flag and HA purifications, nuclear extract was rotated with resin for 4 hours, washed extensively with TAP buffer, and eluted with 0.4 mg/mL of Flag or HA peptide (Sigma). After elution, the complex was TCA precipitated and associated proteins were identified by LC-MS/MS using an LTQ Orbitrap Velos Pro ion-trap mass spectrometer (Thermo-Fisher) and Sequest software.

In vivo PARP inhibitor treatment and histopathological analyses

BRCA1^{+/+}53BP1^{S25A} and WT littermate control mice were administered PARPi (AZD2281) prepared in 10% DMSO/90% Captisol via oral gavage. Mice were treated with 40 mg/kg of PARPi daily in a volume of approximately 100 μ l and monitored daily for changes in health status following PARPi treatment. H&E staining was routinely performed on formalin-fixed, paraffin-embedded tissues. Gut rolls of the small intestine, cecum, and large intestine were digitized with an Aperio ScanScope XT (Leica) at 200 \times in a single z-plane. Aperio whole-slide images were evaluated by a board-certified veterinary pathologist.

Sections were photographed at 10 \times magnification. Mice were perfused transcardially with 4% paraformaldehyde (PFA), while embryos were drop-fixed in 4% PFA and tissues were cryoprotected in 25% PBS-buffered sucrose solution, embedded in O.C.T. and sectioned sagittally at 10 μ m using an HM500M cryostat (Microm). Immunohistochemistry was performed after antigen retrieval.

Antibodies used were: anti-Tbr1 (1:250; Synaptic Systems #328005) and anti-phospho KAP1(Ser-824) (1:500; Bethyl Labs, #A300-767A). Immunostaining of active caspase-3 was visualized with a VIP substrate kit (Vector Laboratories) and biotinylated secondary antibody and avidin-biotin complex (Vectastain Elite kit; Vector Laboratories). Sections were counterstained with 0.1% methyl green (Vector Laboratories), dehydrated and mounted with DPX (Fluka). For fluorescence detection, FITC or Cy3 conjugated secondary antibodies (Jackson Immunologicals) were used and nuclei were counterstained with 4',6-diamidino-2-phenylindole (DAPI) or propidium iodide (Vector Laboratories). TUNEL staining was done using the ApopTag system (Chemicon).

Magnetic Resonance and X-Ray imaging

Magnetic resonance imaging (MRI) was performed using a 7 T Bruker ClinScan system (Bruker BioSpin MRI GmbH, Germany) equipped with 12S gradient coil. A two-channel surface coil was used for MR imaging. Animals were anesthetized and maintained with 1.5%–2% isoflurane during MRI sessions. Data analysis was done by manually segmenting the regions and computing volumes using OsiriX (v5.7, Pixmeo, Switzerland).

For the kyphosis study, mice were imaged in the prone position for a 3-bed position X-ray Computed Tomography (CT) (Inveon Multi-Modality PET/CT, Siemens Medical Solutions, Knoxville, TN). X-ray CT step and shoot acquisition parameters were: 80 kVp, 500 μ A, 1000 msec per step, 180 steps covering 360-degrees. X-ray CT images were reconstructed using a Feldkamp cone beam algorithm with a Shepp-Logan smoothing filter resulting in $512 \times 512 \times 1170$ matrix ($0.08 \times 0.08 \times 0.08$ μ m pixel size). Images were linearly calibrated to Hounsfield units (air: -1000 HU, water: 0 HU). The X-ray CT 3D images (orthogonal axial, coronal, and sagittal views) were displayed using a medical image viewer (MIM v 6.6.5, MIM Software Inc, Cleveland, OH) and a pseudo-3D maximum intensity projection (MIP) was implemented to rotate and translate the mouse into perpendicular orientation for analysis

END-seq and ChIP-SSDS

A retrovirus encoding AsiSI (pTRE3G-HA-ER-AsiSI) was stably transduced into the indicated MEF cell lines as previously described (Canela et al., 2016). Exponentially growing AsiSI-expressing MEFs were treated with 1 μ M doxycyclin (DOX) for 24 hours and then, for 5 hours with 4-OHT, resulting in the nuclear translocation of AsiSI. MEFs were harvested and 9 million cells were embedded in agarose plugs, after which END-seq was performed as described (Canela et al., 2017). END-seq reads were aligned to the mouse (GRCm38p2/mm10) genomes using Bowtie (version 1.1.2) (Langmead et al., 2009) with parameters -n 3 -k 1 -l 50.

Break intensity was measured by integrating the RPKM values within 100 bp of each AsiSI break site. To quantify the width of maximum resection endpoint (in bp), a sliding window containing twenty 100 bp bins was used, starting from the AsiSI site out to 20 kb to the right side. When more than half of the bins within this sliding window had an RPKM value equal to or lower than the background, then the last bin within the window with a detectable signal over background was regarded as the maximum resection endpoint. Background was determined by the maximum END-seq signal for 100 bp bins more than 20 kb (within 20 kb-30 kb) away from individual AsiSI sites.

To map ssDNA bound by RAD51 and RPA at AsiSI sites (ChIP-SSDS), we first captured DNA bound by RAD51 or RPA. Twenty million cells were harvested for chromatin immunoprecipitation (ChIP) using an anti-RAD51 (Abcam #176458, 10 μ g/sample) or anti-RPA antibody (Abcam #10359, 10 μ g/sample). ssDNA that spontaneously forms hairpins after heat renaturation was then enriched and sequenced as described (Brick et al., 2018).

Statistical analyses

Unless indicated, all data are presented as individual replicates. The total number of replicates, mean and error bars are explained in the figure legends. The statistical tests (Mann-Whitney, Welch's, Mantel-Cox and Wilcox Rank Sum) and resulting *P* values (represented by asterisks) are indicated in the figure legends and/or figure panels and were calculated using GraphPad Prism and R software (ns = $p > 0.05$; * = $p \leq 0.05$; ** = $p \leq 0.01$; *** = $p \leq 0.001$; **** = $p \leq 0.0001$).

DATA AND CODE AVAILABILITY

The accession number for the datasets reported in this paper is available at GEO with accession number: GSE133808. <https://www.ncbi.nlm.nih.gov/geo/query/acc.cgi?acc=GSE133808>.